Sym-EFT: Accelerating Effective Field Theory of Large Scale Structure with Symbolic Regression

Despoina Farakou,[1,2]★ Constantinos Skordis,[1,3]†

[1]*CEICO—FZU, Institute of Physics of the Czech Academy of Sciences, Na Slovance 1999/2, 182 00 Prague, Czechia*

[2]*Institute of Theoretical Physics, Faculty of Mathematics and Physics, Charles University, V Holešovičkách 747/2, 180 00 Prague 8, Czechia*

[3]*Department of Physics, University of Oxford, Denys Wilkinson Building, Keble Road, Oxford OX1 3RH, UK*

ABSTRACT

We present an emulator suite for the one- and two-loop cold dark matter power spectrum from the Effective Field Theory of Large Scale Structures (EFTofLSS). Specifically, we emulate separately the various contributions to the one- and two-loop parts of the power spectrum, leaving out the possible counterterms which can be added as multiplicative prefactors. By leaving the time-dependence of the counterterms unspecified at the emulation stage, our technique has the advantage of being extremely versatile in fitting any type of counterterm parametrisation to data, or to simulations, without having to change the emulator. We construct our emulators using the method of symbolic regression which results in functions that can be used directly in computer code, while achieving errors of better than 0.5% within the k-range of validity of EFT and maintaining ultra-fast computational evaluation of less than $\sim 5 \times 10^{-4} s$ on a single core.

Key words: dark matter – Effective Field Theory of Large Scale Structures – emulators – symbolic regression

1 INTRODUCTION

The standard model of cosmology finds observational support from several cosmological surveys. Measurements of the Cosmic Microwave Background (CMB) anisotropies (Bennett et al. 2013; Aghanim et al. 2020; Louis et al. 2025a; Camphuis et al. 2025), observations of the large-scale matter distrubution (Zhao et al. 2021; Chapman et al. 2022; Abbott et al. 2025; Wright et al. 2025) traced by the clustering and weak-lensing of galaxies, and the determination of the expansion rate of the Universe (Scolnic et al. 2018; Brout et al. 2022; Rubin et al. 2023) have provided us with enhanced precision with which the model parameters are estimated. Despite this success, several tensions between the measurement of some of the model parameters by different surveys have persisted (Abdalla et al. 2022), while recent data (Abdul Karim et al. 2025; Lodha et al. 2025; Garcia-Quintero et al. 2025) show possible hints of new physics. As such, accurately constraining our standard model of cosmology remains particularly important.

Current surveys (Gebhardt et al. 2021; Abdul Karim et al. 2025; Mellier et al. 2025; Mandelbaum et al. 2018) are pushing observational precision to new levels, while upcoming surveys (Eifler et al. 2021; Ade et al. 2019; Zhao et al. 2024) will offer a further increase in amount of data, leading to even more precise measurements of the cosmological parameters. Exploiting the data to their full potential requires computing the cosmological model predictions to smaller scales where linear perturbation theory breaks down and the non-linear evolution of dark matter must be taken into account.

N-body simulation methods are the standard and well tested way for precise modelling of observables to small enough scales so that data from surveys can be fully used. In the case of dark-matter-only simulations, the power spectrum computed using different N-body codes has been tested to agree within 1% for wavenumbers $k \lesssim 1h\mathrm{Mpc}^{-1}$ and within 3% for $k \lesssim 10h\mathrm{Mpc}^{-1}$ (Schneider et al. 2016), where h is the dimensionless Hubble constant. However, running N-body simulations is time-costly, and having to run them for several hundreds of thousands of times, as would be necessary when applying Markov chain Monte Carlo (MCMC) to parameter estimation, is prohibitive.

There are two ways to address this limitation. The first approach relies on the use of emulators (Heitmann et al. 2006), which are efficient interpolation methods for reproducing specific observables within a chosen parameter range. Early emulators (Heitmann et al. 2009) of wCDM could reach 1% accuracy for the matter power spectrum for $k \lesssim 1h\mathrm{Mpc}^{-1}$, later widened to 1% for $k \lesssim 10h\mathrm{Mpc}^{-1}$ (Heitmann et al. 2014) up to redshift $z = 4$ using Gaussian process modelling. Later emulators, also based on a Gaussian procces, provided various halo and galaxy clustering statistics (Nishimichi et al. 2019; McClintock et al. 2019b; Zhai et al. 2019; McClintock et al. 2019a) while Giblin et al. (2019), Winther et al. (2019) and Sáez-Casares et al. (2024) provided matter power spectrum emulators in beyond-ΛCDM models, including extensions of general relativity. The Euclid emulator II (Knabenhans et al. 2021) reaches < 1% absolute accuracy in the non-linear power spectrum for $k \lesssim 1h\mathrm{Mpc}^{-1}$ up to $z = 3.5$ with the inclusion of massive neutrinos and parametrized dynamical dark energy. Using neural networks, the BACCO project provided accurate emulators for the dark matter-only power spectrum Angulo et al. (2021) and the baryon boost (Aricò et al. 2021). Finally, six-layer

★ E-mail: farakou@fzu.cz
† E-mail: skordis@fzu.cz

neural networks were used in CosmoPower to emulate all CMB angular power spectra and the matter power spectrum (Spurio Mancini et al. 2021).

The second route is to use higher-order perturbation theory. Linear perturbation theory has been pivotal in the understanding of the cosmic microwave background (CMB) anisotropies, early Universe cosmology, and establishing the concordance ΛCDM model (Dodelson & Schmidt 2020). However, it is expected to become inaccurate around $k \gtrsim 0.1h\text{Mpc}^{-1}$ at $z = 0$ due to the formation of non-linear structures. By including higher-order terms (Jain & Bertschinger 1994; Bernardeau et al. 2002), one can extend the validity of perturbation theory to smaller scales until the non-linear scale $k_{NL} \sim 0.5 - 1h\text{Mpc}^{-1}$, beyond which perturbation theory breaks down and using either N-body simulations, or emulators, seems inevitable. Yet, in this intermediate regime between large and small scales, this theoretical framework can provide additional insights into the Universe's evolution. The Effective Field Theory of Large Scale Structure (EFTofLSS) (Baumann et al. 2012; Carrasco et al. 2012; Hertzberg 2014; Carrasco et al. 2012; Hertzberg 2014; Carrasco et al. 2014a,a,b; Pajer & Zaldarriaga 2013; McQuinn & White 2016), extends standard perturbation theory (SPT) by including the effects of non-linearities at smaller scales and becomes valuable in this context. In EFTofLSS, short-wavelength perturbations can influence large-scale physics through coupling with long-wavelength perturbations (Goroff et al. 1986). Borrowing the analogy from Senatore (2018), similarly to how Maxwell's equations describe the behavior of dielectric materials, the large-scale structure of the Universe can be understood through an EFT up to the non-linear scale. This allows us to derive equations without needing intricate knowledge of the atomic-level structure, in this case galaxy formation, akin to electromagnetism. The effect of integrating out the non-linearities is captured through counter-terms which are time-dependent functions that are otherwise not computable within the EFT.

Given that EFTofLSS necessarily breaks down at the non-linear scale, and also, that with emulators ultra-fast percent-level accuracy can be achieved well beyond its regime of validity, its use may seem an unnecessary step. However, there are good reasons for needing such an EFT. The counter terms capture the short-distance (ultraviolet or 'UV') physics that are to be found when running N-body simulations. Apart from providing the necessary consistency to the theory, it is these counter terms that give the EFTofLSS an edge that neither N-body simulations, nor their emulators, have. These terms can be fitted to N-body simulations (or emulators) and separately to observations, and there is no a priori reason that these fits should agree within a given model, unless it is a good model for our Universe. Hence, with the EFTofLSS one can test a wide range of models, and provide a robust way of parametrically comparing ΛCDM with its various extensions beyond the regime of linear theory.

Nevertheless, while EFTofLSS offers a robust theoretical framework for modeling structure formation, its practical application can be computationally intensive, depending on the loop order used. The CosmoEFT code (Cataneo et al. 2017) can easily take ~ 15 seconds for a single model computation at 1-loop and ~ 16 minutes at 2-loop, both when using 8 cores in high-accuracy settings. While much faster than N-body simulations, it is still somewhat slow for efficient use in MCMC. Several codes have recently achieved $O(\text{second})$ computation while maintaining excellent accuracy (Chudaykin et al. 2020; D'Amico et al. 2021; Linde et al. 2024), however, until recently this was only done for the 1-loop power spectrum and the various 1-loop counterterms relevant for biased tracers. These are currently sufficient for using the EFTofLSS with galaxy surveys. However, it is desirable to have an ultra-fast computation of the 2-loop power

Parameter name	Value	Parameter name	Value
Ω_c	0.2650	$\tilde{A}_s \equiv 10^9 A_s$	2.1005
Ω_b	0.0494	n_s	0.9660
h	0.6732	m_ν	0.06

Table 1. Fiducial cosmological parameters used, see text.

spectrum, as it contributes to CMB lensing at higher redshift and may provide complimentary information. Two-loop accuracy is increasingly relevant to data from CMB experiments; the Atacama Cosmology Telescope (ACT) Louis et al. (2025b), South Pole Telescope (SPT) Ge et al. (2024), and Simons Observatory (SO) Ade et al. (2019) demand high-precision theoretical predictions.

In this work, we build upon these advancements and introduce emulators for the various parts of the EFTofLSS 1- and 2-loop contributions by employing symbolic regression, a machine learning technique that has only recently made its way to cosmology (Bartlett et al. 2024b,a; Sui et al. 2025; Kammerer et al. 2025). Our full emulator is differentiable and achieves sub-millisecond computational speed while maintaining high accuracy, making it suitable for use in large parameter scans or MCMC pipelines. Additionally, we provide a user-friendly interface with the Boltzmann solver CLASS, enabling seamless integration of our EFTofLSS emulator into existing cosmological analysis pipelines. This interface is designed to make the tool easily accessible to the broader cosmology community, facilitating the use of EFTofLSS-based predictions in a wide range of applications.

This article is organised as follows. In Section 2, we describe the EFTofLSS framework at one- and two-loop order. In Section 3, we introduce symbolic regression and describe the construction of our emulator, including dataset generation, and accuracy benchmarks. In Section 3.4, we evaluate the performance ouf our emulator relative to existing tools, and assess its accuracy at higher redshift when applied to CMB lensing. Finally, we conclude in section 4 with a discussion of future directions and applications. The full set of emulators and their validation is collected in appendix-A for one-loop and -B for two-loops. Throughout this paper, we use a fiducial cosmology in our plots; for that, we chose the best-fit cosmology of plikHM_TTTEEE_lowl_lowE_lensing (Aghanim et al. 2020) as shown in Table 1.

2 EFFECTIVE FIELD THEORY OF LARGE SCALE STRUCTURE

2.1 Standard perturbation Theory

We consider a late (spatially flat) Universe cosmology where the only relevant components are that of cold dark matter (CDM), baryons, one species of massive neutrinos of fixed mass $m_\nu = 0.06eV$, and cosmological constant Λ. We denote their relative densities at redshift $z = 0$ as Ω_c, Ω_b, Ω_ν and Ω_Λ respectively, and set the Hubble constant $H_0 = 100h$ km/s/Mpc, where h is the dimensionless Hubble parameter. At $z < 10$ the massive neutrino is already non-relativistic and we can collectively denote the total matter relative density today as $\Omega_m \equiv \Omega_{cb} + \Omega_\nu$, where $\Omega_{cb} \equiv \Omega_c + \Omega_b$ is the relative density of only CDM and baryons, that we use extensively in what follows.

We are interested in descibing the mildly non-linear regime of structure formation using the EFTofLSS. At the lowest approximation the fluctuations of all matter species follow the adiabatic mode so that we may treat them collectively using the adiabatic matter density contrast δ and Eulerian velocity u^i. The effect of baryons has been

treated in Lewandowski et al. (2015) as an additional isocurvature mode and that of neutrinos in Senatore & Zaldarriaga (2017). These make negligible difference at linear scales and can result to few percent differences at higher k.

The first step consists of linear and higher-order fluctuations on the FLRW background above (Bernardeau et al. 2002; Jain & Bertschinger 1994). We neglect vorticity such that u^i is given as a gradient of a scalar $\tilde{\theta}$, i.e. $u_i \equiv \vec{\nabla}_i \tilde{\theta}$. On sub-horizon scales, the density contrast δ and $\tilde{\theta}$ obey the continuity equation

$$\dot{\delta} + \vec{\nabla}_i \left[(1+\delta)\vec{\nabla}^i \tilde{\theta} \right] = 0, \tag{1}$$

and Euler equation

$$\dot{\tilde{\theta}} + \mathcal{H}\tilde{\theta} + \frac{1}{2}|\vec{\nabla}\tilde{\theta}|^2 + \Phi = 0, \tag{2}$$

where a dot denotes differentiation wrt conformal time τ, and $\mathcal{H}$ is the z-dependent conformal Hubble parameter. The gravitational potential Φ which sources (2) is determined from the total matter density via the Poisson equation $2\vec{\nabla}^2\Phi = 8\pi G\bar{\rho}_m\delta$, where $\bar{\rho}_m$ is the background total matter density.

Passing to Fourier space [1], linearizing, and eliminating Φ leads to the two well-known linear continuity and Euler equations

$$\dot{\delta}_1 + \theta_1 = 0, \tag{3}$$

and Euler equation

$$\dot{\theta}_1 + \mathcal{H}\theta_1 + 4\pi G\bar{\rho}_m\delta_1 = 0, \tag{4}$$

where we have introduced the variable $\theta \equiv -k^2\tilde{\theta}$, and the subscript '1' is to mark these variables as corresponding to the linearized fluctuations. The system (3) and (4) has two linearly independent solutions $D^+(\tau)$ and $D^-(\tau)$. In the case $\Omega_m = 1$, these are $D^+ = (z+1)^{-1}$ and $D^- = (z+1)^{-3/2}$ while if $\Omega_m < 1$, D^+ remains a growing mode and D^- a decaying mode. Thus, as it is commonly done, we choose only the growing mode $D^+ = D$ (dropping the '+'), such that $\delta_1 = D\delta_{in}(\vec{k})$ and $\theta_1 = \mathcal{H}\frac{z+1}{z}\frac{d\ln D}{d\ln z}\delta_1$ are given in terms of the same initial condition $\delta_{in}(\vec{k})$.

We now consider higher order terms in (1) and (2) in Fourier space, leading to

$$\dot{\delta} + \theta = -\int\int d^3k_1\, d^3k_2\, \delta^{(3)}\left(\vec{k} - \vec{k}_{12}\right)\frac{\vec{k}_1 \cdot \vec{k}_{12}}{k_1^2}\theta(\vec{k}_1)\delta(\vec{k}_2), \tag{5}$$

and

$$\dot{\theta} + \mathcal{H}\theta + \frac{3}{2}\mathcal{H}^2\Omega_m\delta = -\int d^3k_1 d^3k_2\delta^{(3)}(\vec{k} - \vec{k}_{12})$$
$$\times \frac{k_{12}^2\vec{k}_1 \cdot \vec{k}_2}{2k_1^2 k_2^2}\theta(\vec{k}_1)\theta(\vec{k}_2), \tag{6}$$

respectively, where $\delta^{(3)}$ is the Dirac three-dimensional delta-function, $\vec{k}_{ij} \equiv \vec{k}_i + \vec{k}_j$ and where we have ommitted explicit time dependence in the arguments of δ and θ as well as explicit $\vec{k}$ dependence apart from $\vec{k}_1$ and $\vec{k}_2$.

Equations (5) and (6) form the basis for Eulerian perturbation theory to any order, given the initial condition $\delta_{in}(\vec{k})$ and assumption
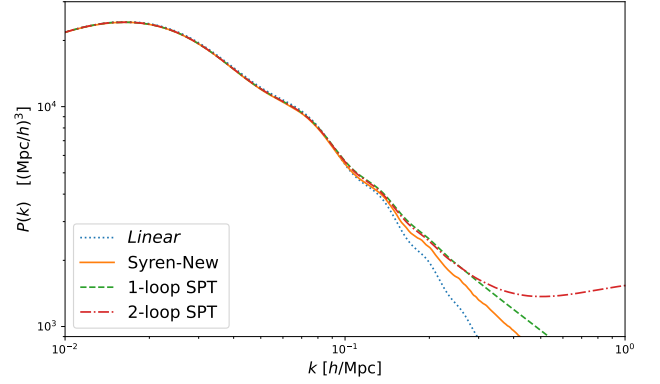

Figure 1. The different contributions to the matter power spectrum. Shown is the linear power spectrum (dotted, blue), 1-loop SPT (dashed, green), 2-loop SPT (dash-dot, red) and the full nonlinear power spectrum from the `Syren-New` emulator (solid, orange).

of growing mode as discussed above. To a good approximation, higher order perturbations may be expanded as a series

$$\delta(\vec{k}, z) = \sum_n D^n\delta_n(\vec{k}), \tag{7}$$

$$\theta(\vec{k}, z) = \mathcal{H}\frac{z+1}{z}\frac{d\ln D}{d\ln z}\sum_n D^n\theta_n(\vec{k}), \tag{8}$$

which enables separating out the time dependance from the k-dependence. These are then used in (5) and (6) to form the solution for δ and θ to any desired order in perturbation theory, in terms of only one initial condition $\delta_1(\vec{k})$ and the growing mode $D(a)$. With this solution at hand, we may form the power spectrum $P(k, a)$ defined by

$$\langle\delta(\vec{k}, z)\delta(\vec{k}', z)\rangle = P(k, z)\delta^{(3)}\left(\vec{k} + \vec{k}'\right). \tag{9}$$

Explicitly in terms of perturbation orders, we may split it into loop corrections, commonly called Standard Perturbation Theory (SPT) terms, as

$$P(k, z) = P_{11} + \underbrace{P_{13} + P_{22}}_{1-loop} + \underbrace{P_{51} + P_{42} + P_{33}}_{2-loop} + \dots \tag{10}$$

where $P_{ij} \sim \langle\delta_i\delta_j\rangle$. The terms on the RHS in (10) are understood to have a k and z dependence, i.e. we have defined the linear power spectrum $P_{11}(k, z)$, the 1-loop SPT power spectrum $P_{1-loop}(k, z) \equiv P_{13}(k, z) + P_{22}(k, z)$ and 2-loop SPT power spectrum $P_{2-loop}(k, z) \equiv P_{51}(k, z) + P_{33}(k, z) + P_{42}(k, z)$ respectively. P_{33} contains two contributions: $P_{33,I}$ which has one loop in each δ_3, and $P_{33,II}$ in which each δ_1 contracts with a δ_1 from the other δ_3.

Interestingly, owing to (7) and (8), the late Universe power spectra factorise, so that we may write

$$P_{11}(k, z) = [D(z)]^2 P_{11}(k) \tag{11a}$$

$$P_{1-loop}(k, z) = [D(z)]^4 P_{1-loop}(k) \tag{11b}$$

$$P_{2-loop}(k, z) = [D(z)]^6 P_{2-loop}(k) \tag{11c}$$

where from now on, we adopt the convention that power spectra without explicit time and k dependence, or with only k-dependence, refer to redshift zero, that is, $P_{11} = P_{11}(k) = P_{11}(k, z = 0)$. Furthermore, when time dependent power spectra are used, the z-dependence will be explicitly written.

We show the various contributions from (10) in Fig.1 contrasted

---

[1] We use the same symbols for position and Fourier space for brevity, since the former is not being used for the remainder of the article. The Fourier convention is that for any variable $A(\vec{x}, t)$ its Fourier space representation is $\int \frac{d^3x}{(2\pi)^3}e^{-i\vec{x}\cdot\vec{k}}A(\vec{x}, t)$.

with the full non-linear result of the `Syren-New` emulator (Sui et al. 2025). While the loop corrections start to be closer to the non-linear power spectrum, over a wider range of scales, they eventually over-predict the power and diverge at smaller scales.

2.2 Effective Field Theory

In the previous subsection, we showed that at very small scales perturbation theory breaks down; see Fig. 1. Thus, we focus on the intermediate scales that can still be described within perturbation theory. It is then useful to split the fields in the Boltzmann equations into short- and long-wavelength parts, $\rho = \rho_l + \rho_s$ and $u^i = u^i_l + u^i_s$, by applying a top-hat filter at a cut-off scale, Λ_{cut}.

Doing so results in a set of equations that involve the long wave-length fields, similar to equations (5) and (6), plus an extra term that is entirely sourced by short modes. The continuity equation:

$$\dot{\rho}_l + 3H\rho_l + \frac{1}{a}\partial_i(\rho_l u^i_l) = 0 \qquad (12)$$

and the Euler equation:

$$\dot{u}^i_l + Hu^i_l + \frac{1}{a}u^j_l(\partial_j u^i_l) + \frac{1}{a}\partial^i\phi_l = -\frac{1}{a\rho_l}\partial_j[\tau^{ij}]_{\Lambda_{cut}} \qquad (13)$$

where $[\tau^{ij}]_{\Lambda_{cut}}$ is the effective stress tensor which originates from the smoothing out of short-wavelength fluctuations (Hertzberg 2014; Carrasco et al. 2012; McQuinn & White 2016; Baumann et al. 2012). The effective stress tensor is a complicated function of all the terms that are allowed by General Relativity, and is non-local in time. In practice, this introduces an imperfect fluid that cancels out the SPT divergences through counterterms, which provide time-dependent functions that further capture the smoothed-out short-scale physics.

It happens that certain infrared (IR) effects, particularly those aris-ing from large-scale displacements, become non-negligible at rele-vant scales and can significantly degrade the accuracy of the results, especially concerning features like Baryon Acoustic Oscillations (BAO). For this reason, it is necessary to perform IR-resummation, which non-perturbatively incorporates these large-scale displace-ments, to obtain accurate predictions for the large-scale structure of the universe (Senatore & Zaldarriaga 2015). The final resumed power spectrum will be given as a sum of the relevant loop terms, times a ker-nel that accounts for the order of resummation. Schematically, each term in the resulting expansion takes the form $\sim C^n[k^{2m}P^{(X_C)}_{L-\text{loop}}]_{\|N}$ where N is the resummation order which depends on the kernel, L is the loop order prior to resummation (with P_{0-loop} being the linear power spectrum P_{11}), C^n are possible counterterms to some power n (if $n = 0$ one is dealing with the SPT part), and (X_C) denotes possible counterterm-specific terms (and is omitted otherwise). We now consider the IR-resumed parts of the power spectrum, up to one and up to two loops.

2.2.1 One-loop EFT

At the one-loop level, the SPT power spectrum of equation (10) has a UV divergence that can be cancelled out by including the sound speed term of the effective fluid (Hertzberg 2014; Baumann et al. 2012; Pajer & Zaldarriaga 2013; Foreman et al. 2015)

$$P^{\text{EFT}}_{1-\text{loop}}(k,z) = \underbrace{[P_{11}(k,z)]_{\|1} + [P_{1-\text{loop}}(k,z)]_{\|0}}_{P^{\text{SPT}}_{1-\text{loop}}(k,z)} + P_{c_s}(k,z) \qquad (14)$$

where $P_{c_s}(k,z)$ is the EFTofLSS counterterm contribution at 1-loop given in terms of the sound speed $c^2_{s(1)}(z)$ as

$$P_{c_s}(k,z) = -2(2\pi)[D(z)]^2 c^2_{s(1)}(z) [k^2 P_{11}]_{\|0}. \qquad (15)$$

where we have conventionally set $k_{NL} = 1h\text{Mpc}^{-1}$. The z-dependent power spectra in (14) are understood to be given following our con-vention explicitly defined through (11). The function $c^2_{s(1)}(z)$ is not determined by the EFT but must be fitted to N-body simulations or to observations, up to a wavenumber k_{fail} which stipulates the breakdown of 1-loop EFT.

2.2.2 Two-loop EFT

The power spectrum up to two loops has a more complicated UV behavior and requires a different set of counterterms (Carrasco et al. 2014b,a; Foreman et al. 2015).

$$P^{\text{EFT}}_{2-\text{loop}}(k,z) = \underbrace{[P_{11}(k,z)]_{\|2} + [P_{1-\text{loop}}(k,z)]_{\|1} + [P_{2-\text{loop}}(k,z)]_{\|0}}_{P^{\text{SPT}}_{2-\text{loop}}(k,z)}$$
$$+ (2\pi)c^2_{s(1)} \left([P^{(\text{cs})}_{1-\text{loop}}(k,z)]_{\|0} - 2[k^2 P_{11}(k,z)]_{\|1}\right)$$
$$- 2(2\pi)c^2_{s(2)}[k^2 P_{11}(k,z)]_{\|0} + (2\pi)c_1[P^{(\text{quad})}_{1-\text{loop}}(k,z)]_{\|0}$$
$$+ (2\pi)^2 \left[\left(c^2_{s(1)}\right)^2\left(1 + \frac{2\zeta + 5}{4\zeta + 5}\right) + 2c_4\right][k^4 P_{11}(k,z)]_{\|0} \qquad (16)$$

where once more we have conventionally set $k_{NL} = 1h\text{Mpc}^{-1}$, and ζ is a constant parameter. At 2 loops new counterterms emerge in addition to $c^2_{s(1)}(z)$, and these are the time-dependent functions $\{c^2_{s(2)}(z), c_1(z), c_4(z)\}$. These terms are in general non-local in time, however, local versions can be constructed approximately.

The factorisation of all terms appearing in (14) and (16) into separate functions z and k, see (11), is what motivates our emulation strategy in what follows. More importantly, the counter terms are left outside of the emulation scheme and are expected to be supplied as external functions by the user.

3 SYMBOLIC REPRESENTATION OF EFTOFLSS

3.1 Symbolic regression

There is no faster way of approximating the output of a numerical algorithm, in our case the power spectrum, than by using an explicit functional form. Furthermore, explicit functions can be inserted into any computer code quite easily, and offer an interpretable and fully differentiable way of interpolating, and in our case emulating the desired power spectra.

Such explicit functional forms, in other words fitting functions, have traditionally been used in cosmology for this purpose. Old examples include, the CDM transfer function fit of Bond & Efstathiou (1984), the CDM, WDM and massive neutrino transfer function fits of Bardeen et al. (1986), the non-linear matter power spectrum fit of Peacock & Dodds (1994) and the physics-informed improvement of Eisenstein & Hu (1998). While these functions have served their purpose by providing sufficient accuracy at the time, the very high precision that is necessary now and the shear number of terms that need interpolation makes this task humanly impossible.

Symbolic regression is a supervised machine learning method which generates explicit mathematical expressions that can be used to model a given dataset. In contrast with other regression methods
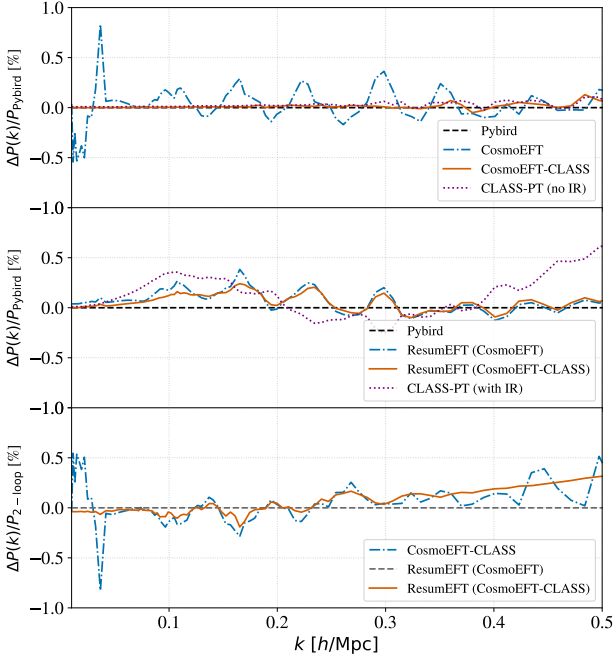
Figure 2. *Top:* $P^{\mathrm{SPT}}_{1-\mathrm{loop}}(k)$ %-relative difference of `CosmoEFT` (dash-dot, blue), `CosmoEFT-Class` (solid, orange) and `CLASS-PT` (dotted, purple) compared respectively with `Pybird`(baseline, dashed black). *Middle:* IR-resummed $P^{\mathrm{SPT}}_{1-\mathrm{loop}}(k)$ %-relative difference of `CosmoEFT` (dash-dot, blue), `CosmoEFT-Class` (solid, orange) and `CLASS-PT` (dotted, purple) compared with `Pybird`(baseline). *Bottom:* Comparison between the 2-loop SPT power spectrum $P^{\mathrm{SPT}}_{2-\mathrm{loop}}(k)$ with and without IR resummation. Shown is the %-relative difference between the baseline model (IR-resummed `CosmoEFT`) and `CosmoEFT` prior to resummation (dash-dot, blue), and with `CosmoEFT-Class`(solid, orange) with resummation.

where the functional form is fixed and optimisation takes place only on the free parameters, in symbolic regression the structure of these functions is also unknown and is part of the optimisation procedure. How well a functional form fits the data is encapsulated in a "loss" function, and the task of a symbolic regression algorithm is not only to minimise the loss function, but may also be to select expressions of smaller length to avoid over-fitting and enable generalization. As such, one implements a multi-objective strategy.

A commonly used approach to symbolic regression is by applying Genetic Programming (Koza 1992), a method inspired by natural selection. In the context of symbolic regression, expressions are drawn from a pool and manipulated through either cross-breeding or through mutation. The ones which fit better are then retained and after several generations, more accurate expressions of various lengths are produced. The two-dimensional plot of accuracy versus expression length is called the Pareto front, and it signifies the most optimal set of expressions found until the moment the algorithm was terminated.

Several implementations of symbolic regression exist. We chose the `Operon` framework (Burlacu et al. 2020) which implements symbolic regression using genetic programming. Written in C++ and publicly available [2], it is based on a compact and efficient linear

tree encoding and indexing scheme for representing expressions, it internally uses dual numbers for auto differentiation, has low memory footprint and is highly parallel. It has been shown to scale well to evolving over 10^6 individual expressions depending on multidimensional parameter spaces. A comparison of several symbolic regression codes, including some which use a different method than genetic programming, may be found in Cava et al. (2021). It is found that 4 out of 5 top performers are based on genetic programming and `Operon` is at a sweetspot on the Pareto front of models in terms of simplicity and accuracy of produced expressions. Finally, in Radwan et al. (2024) it was demonstrated that genetic programming is still superior compared to modern implementations of symbolic regression using deep generative neural networks. [3]

Symbolic regression has recently been used in cosmology to emulate the linear power spectrum (Bartlett et al. 2024b), non-linear dark matter power spectrum (Bartlett et al. 2024a; Sui et al. 2025), the baryon boost to the matter power spectrum (Kammerer et al. 2025), as well as the growth rate and comoving distance (Bartlett & Pandey 2025).

3.2 EFTofLSS codes: generating the dataset

We computed the terms of the EFTofLSS power spectrum in (14) and (16) using the `CosmoEFT` C++ code (Cataneo et al. 2017) and passed the result through the `ResumEFT` code (Cataneo et al. 2017) for performing the IR resummation [4]. Since we were not concerned with speed when generating the datasets, we set $\Lambda_{IR} = 0.1$ in `ResumEFT` to increase accuracy. The `CosmoEFT` code takes as input a set of cosmological parameters and the linear matter transfer function. For efficient calculation of the EFTofLSS terms, `CosmoEFT` uses internaly the `COPTER` code (Carlson et al. 2009) which provides IR-safe integrands (Carrasco et al. 2014a) and computes the loop integrals using Monte Carlo integration routines from the CUBA library (Hahn 2005). Moreover, it is set to use a fiducial cosmology that is computed once (by the code) and used to calculate the desired power spectra for other cosmologies which are close enough, accelerating the computation while maintaining fair precision. Since in our case, speed was not a concern at the computation stage, we instead bypassed the fiducial cosmology and let the code to always compute the power spectra from scratch. Moreover, we interfaced `CosmoEFT` with the Boltzmann code `CLASS` (Blas et al. 2011) and passed it the exact numerically calculated background and linear cosmology directly. Thus, the resulting `CosmoEFT-Class` code was able to provide more accurate spectra in order to have better precision when coupling it to `Operon`. After tuning its precision parameters, the code reported estimated errors $\sim 0.1\%$ which we have taken as the base value.

Other codes for computing the 1-loop EFTofLSS power spectra [5] include Class-PT (Chudaykin et al. 2020), Pybird (D'Amico et al.

---

https://github.com/heal-research/pyoperon or https://pypi.org/project/pyoperon/.

[3] Nevertheless, genetic programming is not by itself an efficient method for implementing symbolic regression (Kronberger et al. 2024), as a large portion of visited expressions are of low quality, and several of them are semantically equivalent to previously visited expressions. Thus, there is still a lot of room for improving the techniques, although we note that symbolic regression has been shown to be an NP-hard problem (Virgolin & Pissis 2022).

[4] These codes used to be publicly available at http://web.stanford.edu/~senatore/ which no longer exists.

[5] Pybird is publicly available at https://github.com/pierrexyz/pybird while the Class-PT code can be found from https://github.com/Michalychforever/CLASS-PT. Class-OneLoop is not yet public.

2021) and Class-OneLoop (Linde et al. 2024), which in addition to the 1-loop matter power spectrum compute correlators for biased tracers. These codes are generally faster than CosmoEFT, however, they do not provide the 2-loop matter power spectrum needed here.

We compare $P_{1-\text{loop}}^{\text{SPT}}$ from (14) of the matter power spectrum from CosmoEFT, CosmoEFT-Class, Pybird and CLASS-PT in Fig.2, without IR resummation (top panel) and with IR resummation (middle panel). We see that without IR resummation the difference between Pybird, CLASS-PT and CosmoEFT-Class is negligible until $k \sim 0.5h\text{Mpc}^{-1}$ (within 0.1%) while CosmoEFT differs at the 0.5% level – the difference is largely due to the use of the fiducial cosmology in CosmoEFT, and its internal use of COPTER which does not account for massive neutrinos. We note that performing the comparison between CosmoEFT and CosmoEFT-Class without massive neutrinos reduces the difference significantly.

Switching on IR resummation increases the difference between Pybird and CosmoEFT-Class to $\sim 0.25\%$. While we tried increasing the accuracy settings of both codes at the cost of speed, and also varied the Λ_{IR} parameter, we were unable to reduce this difference [6]. In the CLASS-PT case, we see larger differences reaching $\sim 0.5\%$ and growing to over 2% at $k \sim 0.8h\text{Mpc}^{-1}$. This larger difference in CLASS-PT is related to the IR resummation scheme. In doing both comparisons, with and without IR resummation, we had adjusted the 1-loop sound speed to a small non-zero value to align the power spectra, after having observed a difference proportional to $[k^2 P_{11}(k)]_{\|0}$. A more detailed comparison of all the EFT codes is left for a future, more dedicated study.

Although no other 2-loop code apart from CosmoEFT was available to us, we performed an *internal* comparison between CosmoEFT and CosmoEFT-Class at the bottom panel of Fig.2, with and without IR resummation. This shows that the CosmoEFT method of using a fiducial cosmology and then computing the desired spectra for cosmologies which are close enough to this fiducial cosmology can introduce an error of $\sim 0.25\%$ at $k \lesssim 0.4h\text{Mpc}^{-1}$, increasing to 0.5% at larger k, with or without IR resummation.

3.3 The emulators

We used CosmoEFT-Class and ResumEFT to generate our training set of 200 cosmologies drawn from the set of parameters $\{\tilde{A}_s, \Omega_{cb}, \Omega_b, h, n_s\}$, where $\tilde{A}_s \equiv 10^9 A_s$. We sampled these with a Latin hypercube within the same range as for Syren-New (Sui et al. 2025) and the Euclid emulator II (Knabenhans et al. 2021), shown in Table 2. The codes return all the individual terms entering the 1-loop (14) and 2-loop (16) power spectra. The full set is listed in Table 3. We kept a fixed 114 k-values for all models between $k = 0.01h\text{Mpc}^{-1}$ and $k_{max} = 3.3h\text{Mpc}^{-1}$, log-spaced, but with more points where EFTofLSS is relevant, which is $0.05 < k < 1h\text{Mpc}^{-1}$. For validation, we generated a further 100 cosmologies from the same set, however, at different points in parameter space and sampled on the same k values as with the training set. Since our k values are densely populated and given that functions generated by Symbolic regression are typically smooth, we expect fluctuations between k values to be small. Furthermore, in several cases we found it more efficient to normalize the EFT functions tabulated in Table.3 with some convenient known functional combination to achieve faster convergence of the emulator. The training set is shown collectively in Fig.3.

While the genetic programming algorithm of Operon is completely deterministic, the output does depend on the initial ran-

---

[6] We thank Pierre Zhang for discussions on this issue and help with Pybird.

Parameter	Lower bound	Upper bound
Ω_m	0.24	0.4
Ω_b	0.04	0.06
h	0.61	0.73
$\tilde{A}_s \equiv 10^9 A_s$	1.7	2.5
n_s	0.92	1

Table 2. Cosmological parameter ranges used for generating our training sets. We also kept two massless neutrinos and one massive with $m_\nu = 0.06eV$.

1-loop	2-loop	Notes
$[k^2 P_{11}(k)]_{\|0}$	$[k^2 P_{11}(k)]_{\|1}$	
$[P_{11}(k)]_{\|1}$	$[P_{11}(k)]_{\|2}$	
-	$[k^4 P_{11}(k)]_{\|0}$	
$[P_{1-\text{loop}}(k)]_{\|0}$	$[P_{1-\text{loop}}(k)]_{\|1}$	Three regions each
-	$[P_{2-\text{loop}}(k)]_{\|0}$	Two regions
-	$[P_{1-\text{loop}}^{(\text{cs})}(k)]_{\|0}$	
-	$[P_{1-\text{loop}}^{(\text{quad})}(k)]_{\|0}$	

Table 3. Emulated functions for 1-loop and 2-loop EFTofLSS terms.

dom seed. Thus, it may happen that the generated expressions were not of sufficient quality, and this is not easy to control beforehand (cf. footnote 3). Therefore, we run Operon for few different hyperparameters, namely, $\epsilon = \{10^{-3}, 10^{-4}\}$, 'maximum selection pressure'$= \{80, 100\}$, 'population size'$= \{1000, 1500\}$, 'tournament size'$= \{5, 10\}$, 'optimizer iterations'$= \{8, 9, 10\}$ and 'pool size'$= \{100, 150\}$. Furthermore, we run ~ 10 different initial random seed numbers keeping the same hyperparameters and collected the best expressions found after all these runs had finished.

Expressions generated by Operon can very often be simplified further, for example, by combining constants together. Moreover, Operon optimizes all the coefficients in the expressions it determines to machine precision by default. However, since our error tolerance is larger, we reduced the significant figures of each constant in our chosen expression up to the point that the error would start to change by an amount larger than 10^{-3}. This process may result to slight reductions to the expression length compared to that reported by Operon and displayed in the Pareto fronts.

To make the emulators more useful, we have tried to make the emulation error as small as possible. However, noticing that the differences between one-loop EFT codes are within 0.5%, as discussed above and seen in Fig.2, it makes little sense to reduce the error to smaller values. Thus we set our emulation error target to $\sim 0.5\%$.

3.3.1 The 1-loop emulators

At 1-loop we have the following 3 functions: $[k^2 P_{11}(k)]_{\|0}$, $[P_{11}(k)]_{\|1}$ and $[P_{1-\text{loop}}(k)]_{\|0}$, the first one being used for the $c_{s(1)}^2$ counterterm and the latter two forming $P_{1-\text{loop}}^{\text{SPT}}$.

Consider first $[k^2 P_{11}(k)]_{\|0}$. The functional form of this term is fairly close to the bare linear spectrum multiplied by k^2, that is, $k^2 P_{11}(k)$, upto $O(1)$ deviations. Thus it is far more efficient to emulate instead their ratio $E_{cs^2}^{(1)} \equiv \frac{[k^2 P_{11}]_{\|0}}{k^2 P_{11}}$, shown in panel '(a)' of Fig.3. The resulting Pareto front of the Root Mean Square Error (RMSE) vs expression length is shown on the left panel of Fig. 4. We chose an expression of length 50, which after our reduction process
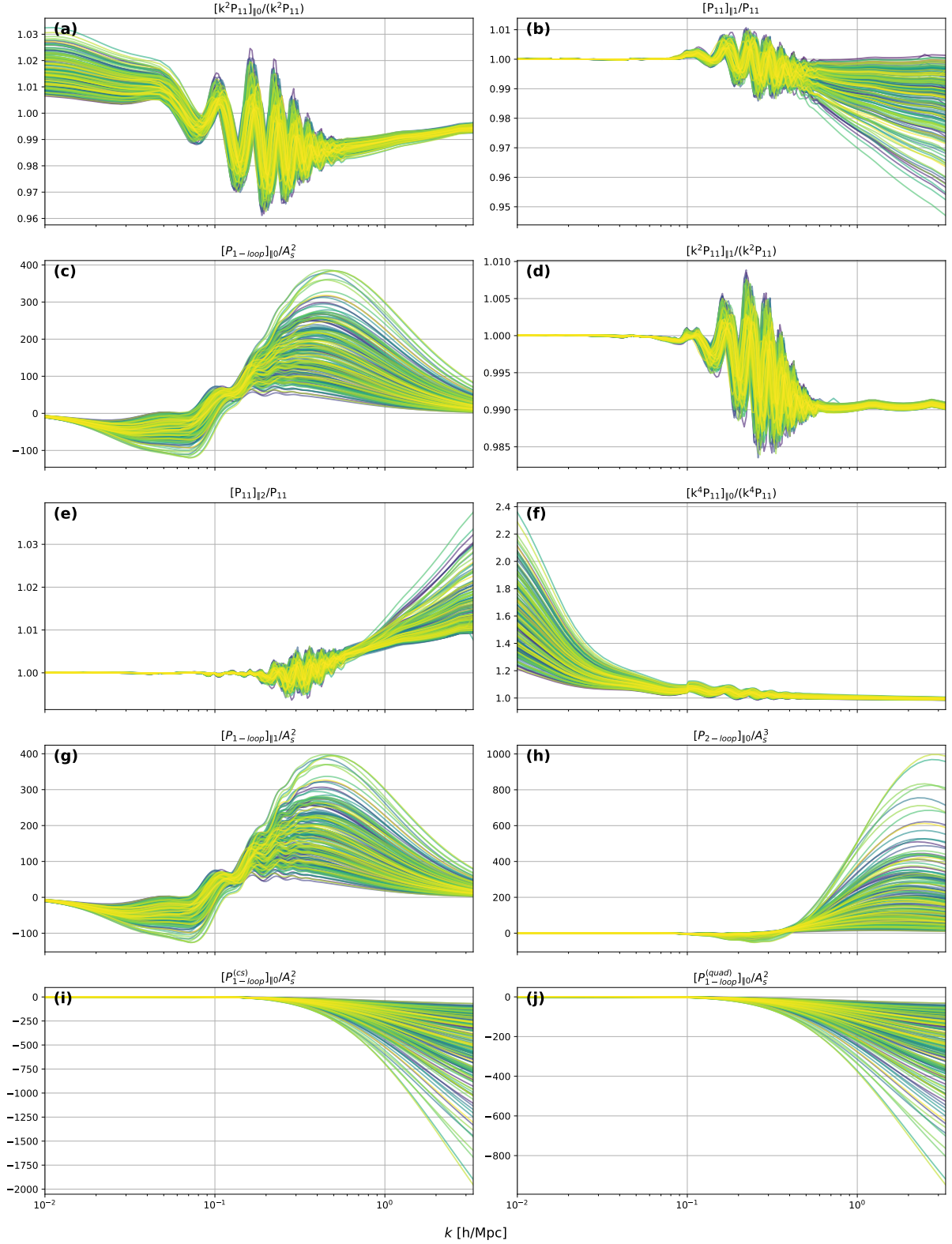
Figure 3. Training Data for 200 cosmologies. Each line corresponds to a specific set of cosmological parameters, sampled with a Latin hypercube within the bounds in Table. 2

described above, takes the form

$$
\begin{aligned}
E_{cs^2}^{(1)} =& C_{19} + \left\{ \Omega_{cb} \left[C_{12}h - \cos\left(C_{13}\tilde{A}_s\right) \right] - C_{14}\Omega_b \right\} \\
&\times \left(\frac{C_{15}}{\sqrt{C_{16}k^2 + 1}} - \frac{C_{17}}{\sqrt{C_{18}k^2 + 1}} \right) \\
&- \frac{(C_0\Omega_b - C_1 k)\cos\left(C_6 k + \frac{k(C_2 h + C_3)}{\sqrt{k^2 + (C_4\Omega_{cb} + C_5\Omega_b)^2}} + \ln\left(C_7 k\right)\right)}{\sqrt{\left(C_8\tilde{A}_s + \frac{\frac{C_{10}\Omega_{cb}}{k} - C_9\tilde{A}_s}{\sqrt{C_{11}k^2 + 1}}\right)^2 + 1}}
\end{aligned}
$$
(17)

where the coefficients are

$$
\begin{array}{llll}
C_0 = 0.709 & C_5 = 10.322 & C_{10} = 1.813 & C_{15} = 0.1188, \\
C_1 = 0.059 & C_6 = 55.1 & C_{11} = 0.015 & C_{16} = 249, \\
C_2 = 52.48 & C_7 = 6.125 & C_{12} = 3.395 & C_{17} = 0.0609, \\
C_3 = 23.42 & C_8 = 1839.487 & C_{13} = 0.472 & C_{18} = 5.68, \\
C_4 = 3.305 & C_9 = 1840.901 & C_{14} = 3.9 & C_{19} = 0.99508.
\end{array}
$$
(18)

Our choice was informed by inspecting the final emulation error on the 1-loop spectrum, as smaller expressions were not reducing the emulation error within out target threshold. We return to this issue in the discussion and conclusion section below.

We turn now to the $[P_{11}]_{\|1}$ part of the spectrum. In this case, it is better to emulate the ratio $[P_{11}]_{\|1}/P_{11}$, shown in panel '(b)' of Fig.3, which removes the variation of P_{11} over three orders of magnitude. The resulting emulator of length 50 and its coefficients as well as the Pareto front are shown in appendix A.

The final part of the 1-loop spectrum is the function $[P_{1loop}]_{\|0}$, normalized by dividing wth $\tilde{A}_s^2$. This function has proven to be more difficult to emulate due its large variation from very negative to very large and positive values, in addition to the squeezed part around $k \sim 0.1 h\mathrm{Mpc}^{-1}$ which shows less variation between the different cosmologies. Thus, to achieve better precision we split the $[P_{1loop}]_{\|0}$ function into three overlapping regions in k-space. We checked various ways to split the regions and found that the best choice resulting in lower errors is the one described below.

Our choice was motivated as follows. On very small scales the dominant term in the power spectrum is P_{11} (and its IR resummations), and so we defined the first region as $k = [0.01, 0.3] \times h\mathrm{Mpc}^{-1}$. In the second region we require high precision in the EFTofLSS contribution which has to perform well to higher k and so we chose $k = [0.2, 1.] \times h\mathrm{Mpc}^{-1}$, to allow overlap with region 1. In the third region the integrals for all cosmology seem to have a similar decaying behavior, see panel '(c)' of Fig.3, and we chose this to be $k = [0.9, 3.3] \times h\mathrm{Mpc}^{-1}$. Even though the EFT is expected to fail already around $k_{\mathrm{fail}} \sim 0.4 h\mathrm{Mpc}^{-1}$ at redshift zero, having the spectra out to higher k is necessary as k_{fail} increases with increasing redshift. This does not mean, however, that the higher-loop contributions are more important at higher redshift; rather, the higher-loop contributions are also multiplied by higher power of $D(z)$ and thus, also more suppressed at higher redshift relative to the linear spectrum.

We created three emulators, one for each region, corresponding to $[P_{1loop}]_{\|0}$. Our chosen functions have lengths 70, 83 and 50 respectively, and are shown in appendix A, along with their corresponding Pareto fronts generated by Operon in Fig. A2. While we have tried to choose smaller and thus simpler expressions, our primary measure was accuracy, which meant that choosing smaller expressions would not lead to our 0.5% error target. To create the full emulator for $[P_{1loop}]_{\|0}$, we joined these three functions along their respective

overlap intervals, using the error function $\mathrm{Erf}\left[C_n(k_n - k)\right]$, where C_n and k_n are constants indexed by the left region. Specifically for the joining of regions 1 and 2 we set $C_1 = 100$ and $k_1 = 0.25$, while for joining regions 2 and 3 we set $C_2 = 40$, $k_2 = 0.95$. While one would expect that the joining would be dependent on the cosmological parameters, in practice this is not necessary, and this leads to a simpler implementation.

On the left panel of Fig.5 we show the emulated $[P_{1loop}]_{\|0}$ for one set of cosmological parameters, indicating the three constituent emulators in blue, orange and grey (from large to small scales) and how they join within each overlapping region to produce the full emulated function. The boundaries of the overlapping regions are marked by vertical lines. We use dashed lines to show how each emulator extrapolates outside their respective region, however, in practice we set the extrapolated part explicitly to zero.

3.3.2 2-loop Symbolic-EFTofLSS

We now turn to the IR-resummed 2-loop power spectra as they appear in (16). There are 7 functions to emulate, see Table. 3. Consider first the resummed $[k^2 P_{11}]_{\|1}$ function which is derived from the linear spectrum P_{11} and is part of the $c_{s(1)}^2$ counterterm contrubution to the 2-loop power spectrum. Just as in the $[k^2 P_{11}]_{\|0}$ case of the previous subsection, it is far more efficient to emulate the ratio $\frac{[k^2 P_{11}]_{\|1}}{k^2 P_{11}}$, as is easily seen from panel '(d)' of Fig.3. We show the RMSE vs model length Pareto front on the left panel of Fig.6 with blue marking the training and red the validation error. Even though Operon found models resulting in 8 times smaller error, we chose a function with model length 25 as it was sufficient to pass our error targets. The resulting emulator is given by

$$
\begin{aligned}
\frac{[k^2 P_{11}]_{\|1}}{k^2 P_{11}} =& C_0 + \frac{1}{\sqrt{C_{10}k^{C_{11}} + 1}} \Bigg[C_8 \cos(C_9 k) \\
&- \frac{C_1\Omega_b \cos(C_2\Omega_{cb} + C_3\Omega_b - C_4 h - C_5 k)}{\sqrt{\frac{C_6}{k^{C_7}} + 1}} \Bigg]
\end{aligned}
$$
(19)

where the coefficients are

$$
\begin{array}{lll}
C_0 = 0.99072 & C_4 = 3.9 & C_8 = 9.218 \times 10^{-3} \\
C_1 = 0.132 & C_5 = 95.5 & C_9 = 3.44 \\
C_2 = 19.23 & C_6 = 10^{-6} & C_{10} = 5.6 \times 10^4 \\
C_3 = 63 & C_7 = 8.24 & C_{11} = 9.9
\end{array}
$$
(20)

This was by far the simplest emulator we have constructed. Notice that there is no dependence on either the amplitude $\tilde{A}_s$ nor the spectral index n_s, while the other three cosmologicical parameters, Ω_m, Ω_b and h, appear only in the second cosine function, whose amplitude is modulated by Ω_b. Interestingly, the double k-dependent envelope given by the two square roots has no dependance on the cosmological parameters – it is universal.

There are two further functions derived from the linear spectrum P_{11}. These are the IR-resummed $[P_{11}]_{\|2}$ which is part of $P_{2-\mathrm{loop}}^{\mathrm{SPT}}$ and $[k^4 P_{11}]_{\|0}$ which relates to the $c_4(z)$ counterterm. Just as the previous function, it is more efficient to emulate the ratios $\frac{[P_{11}]_{\|2}}{P_{11}}$ and $\frac{[k^4 P_{11}]_{\|0}}{k^4 P_{11}}$, shown in panels '(e)' and '(f)' of Fig.3, respectively. The resulting RMSE vs model length Pareto fronts are shown in appendix B, left panel of Fig.B1 and Fig.B2, respectively. The chosen expressions have lengths 44 and 70, respectively, in order to be within
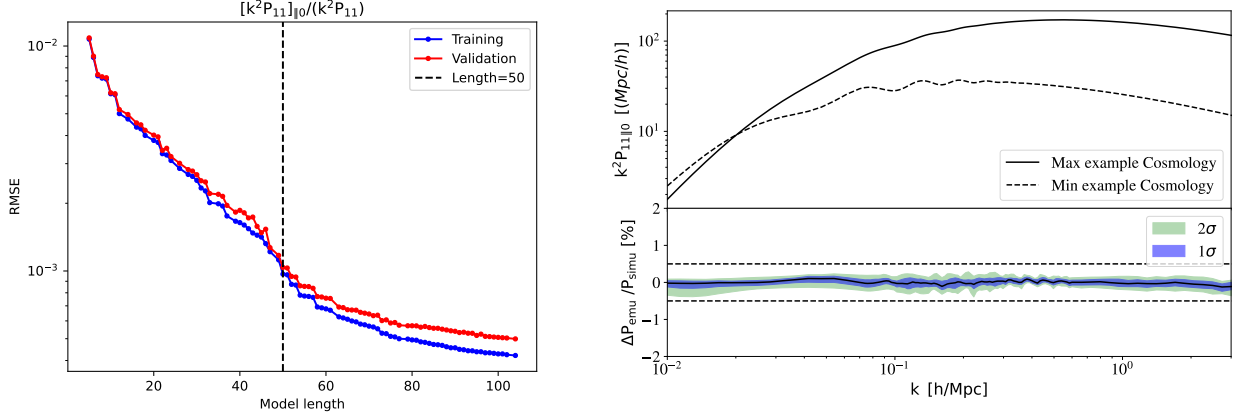
Figure 4. *Left:* The Pareto front of RMSE vs model length for the $\frac{[k^2 P_{11}]_{\parallel 0}}{k^2 P_{11}}$ emulator runs as generated by `Operon`, with blue marking the training and red the validation error, and with the chosen model of length 50 indicated by the vertical dashed line. *Right:* The top plot shows the $[k^2 P_{11}]_{\parallel 0}$ function for two extreme cases of cosmological parameters while the bottom plot displays the resulting 1σ and 2σ emulator % error for all 300 cosmologies. The horizontal dashed lines mark the 0.5% threshold.

Figure 5. *Left:* The $[P_{1-\mathrm{loop}}]_{\parallel 0}$ power spectrum for one set of cosmological parameters, split in three overlapping regions whose boundaries are marked with vertical lines. We plot each emulated function within its region with a solid line, and outside its region of validity with a dashed line. *Right:* The $[P_{2-\mathrm{loop}}]_{\parallel 0}$ power spectrum, split in two overlapping regions, whose boundaries are marked with vertical lines. We use the same plotting conventions as the left panel.

our error threshold, as shown on the right panels of Fig.B1 and Fig.B2.

We now turn to the $[P_{1-\mathrm{loop}}]_{\parallel 1}$ spectrum, displayed in panel '(g)' of Fig.3, normalized further by dividing with $\tilde{A}_s^2$. This function has a striking resemblance to $[P_{1-\mathrm{loop}}]_{\parallel 0}$, as they are both IR resummations of the same underlying function $P_{1-\mathrm{loop}}$, hence, we adopted the same emulation procedure as for the latter. To summarise, we split it into the same three regions in k-space as in Sec.3.3.1 and emulated each region separately, joining the resulting functions as above. The Pareto fronts and chosen equations are displayed in appendix B3.

Next in line is the $[P_{2-\mathrm{loop}}]_{\parallel 0}$ term, normalized by dividing with $\tilde{A}_s^3$ and shown in panel '(h)' of Fig.3. While this function is markedly different from both the $[P_{1-\mathrm{loop}}]_{\parallel 0}$ and $[P_{1-\mathrm{loop}}]_{\parallel 1}$ cases, it exhibits similar difficulty in emulation because of its 3 orders of magnitude rise on scales smaller than $k \gtrsim 0.4h\mathrm{Mpc}^{-1}$ after first having gone through negative values on larger scales. However, in this case having just two overlapping regions was sufficient. We chose the first region to be $k = [0.01, 0.5] \times h\mathrm{Mpc}^{-1}$ and the second as $k = [0.4, 3.3] \times$

$h\mathrm{Mpc}^{-1}$, having tried different possibilities and finding that this combination was better at minimizing the error and capturing the features of the underlying $[P_{2-\mathrm{loop}}]_{\parallel 0}$ function. The Pareto fronts resulting from the `Operon` runs are shown in Fig.B4 of appendix B4, along with the chosen equations of lengths 65 and 70 respectively. Joining of the two regions was done using the error function as in Sec.3.3.1 but with different parameters set to $C_1 = 100$ and $k_1 = 0.4$.

The final 2-loop functions that we emulate are the IR resummed $[P_{1-\mathrm{loop}}^{(\mathrm{cs})}]_{\parallel 0}$ and $[P_{1-\mathrm{loop}}^{(\mathrm{quad})}]_{\parallel 0}$, shown in panels '(i)' and '(j)' of Fig. 3, respectively. These display similar behaviour of ~ 3 orders of magnitude rise on small scales. with the former being around three times larger. Both display features on large scales which are not visible in the plot, and one strategy would have been to split the k interval in at least two regions, as we have done in the other cases above. However, we decided not to, given that for $k \lesssim 0.3h\mathrm{Mpc}^{-1}$ their contribution to the total $P_{2-\mathrm{loop}}^{\mathrm{EFT}}$ is negligible. This is seen on the top panel of Fig.B5 and Fig.B6. Emulating the entire range and choosing models of length 78 and 72 respectively –see the left panels of
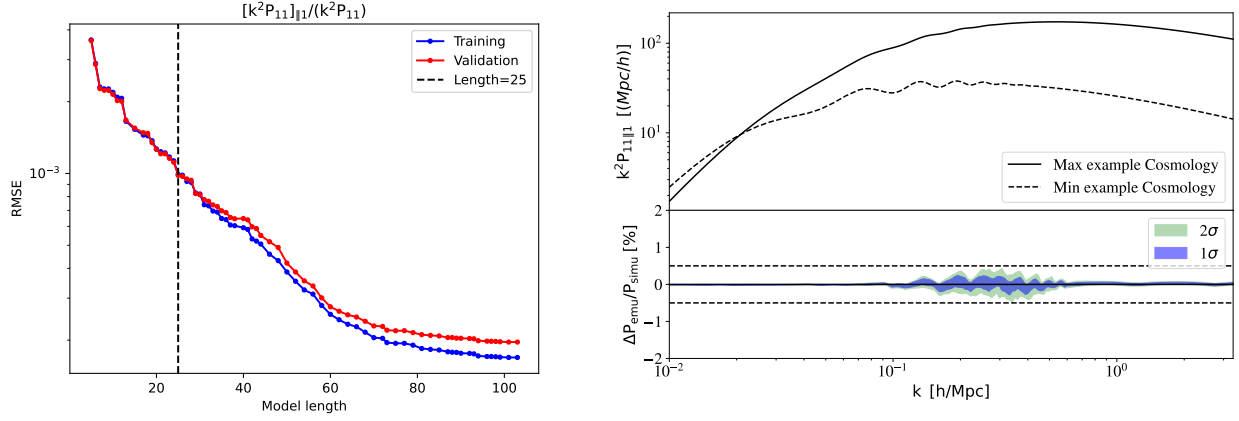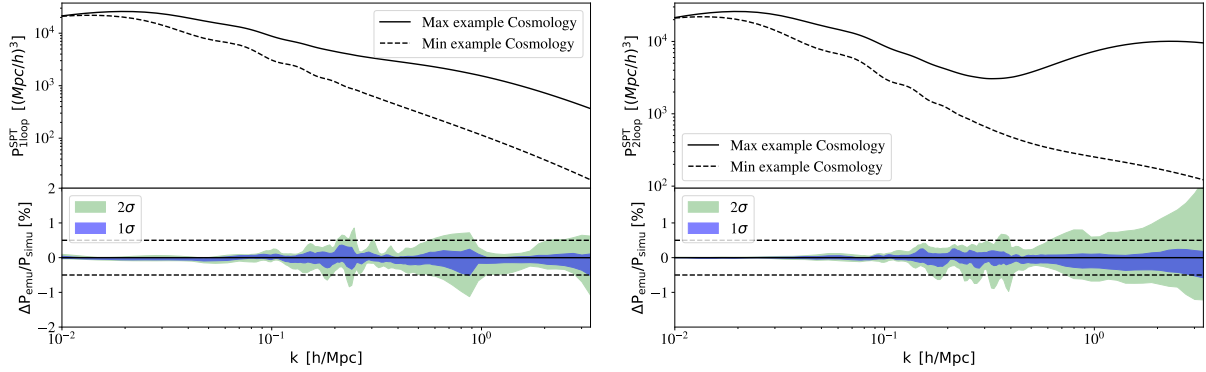
Figure 6. *Left:* The Pareto front of RMSE vs model length for the $\frac{[k^2 P_{11}]_{\|1}}{k^2 P_{11}}$ emulator runs as generated by `Operon`, with blue marking the training and red the validation error, and with the chosen model of length 25 indicated by the vertical line. *Right:* The top plot shows the $[k^2 P_{11}]_{\|1}$ function for two extreme cases of cosmological parameters while the bottom plot displays the resulting 1σ and 2σ emulator % error for all 300 cosmologies. The horizontal dashed lines mark the 0.5% threshold.

Figure 7. *Left:* The top plot shows the P_{1-loop}^{SPT} function for two extreme cases of cosmological parameters, while the bottom plot displays the resulting 1σ and 2σ emulator % error. The horizontal dashed lines mark the 0.5% threshold. *Right:* The top plot shows the P_{2-loop}^{SPT} function for two extreme cases of cosmological parameters, while the bottom plot displays the resulting 1σ and 2σ emulator % error. The horizontal dashed lines mark the 0.5% threshold, same as the left plots.

Fig.B5 and Fig.B6 for the Pareto fronts– leads to error less than 0.5% within the relevant range. We have checked that the large error for $k \lesssim 0.3h\mathrm{Mpc}^{-1}$ does not translate to large errors in the full $P_{2-\mathrm{loop}}^{\mathrm{EFT}}$.

3.4 Error comparison

Having presented all our emulators, let us now assess the overall error and how the combined emulators fare against other existing codes. We first tested the error by keeping within the SPT part of either 1-loop or 2-loops, that is, setting all the counterterms to zero. We show the results in the left (1-loop) and right (2-loop) panels of Fig.7. The top part of each panel shows two extreme cases of how the total SPT function looks like. While both extremes are practically intersecting around $k \sim 0.01h\mathrm{Mpc}^{-1}$, they are widely disparate on small scales upto a factor of ~ 10 for the 1-loop and ~ 100 for 2-loop spectrum. Yet, despite these large variations, the %-error remains within our 0.5% threshold for the whole range of k at 1σ, and with few deviations outside 0.5%, but still within $\sim 1\%$ at 2σ for $k \lesssim 2h\mathrm{Mpc}^{-1}$. At larger k, the 2σ 1-loop error remains within 1%,

dominated by the $[P_{1-\mathrm{loop}}(k)]_{\|0}$, while at 2-loops it reaches $\sim 2\%$ at $k \sim 3h\mathrm{Mpc}^{-1}$, dominated by the $[P_{2-\mathrm{loop}}(k)]_{\|0}$ part. However, this is outside the regime of validity of EFT at $z = 0$ while at high enough redshift when EFT is valid there, it will be suppressed by higher powers of the growth factor $D(z)$ and thus we do not expect this to be an issue.

Let us now compare our `Sym-EFT` emulator with other codes for several sets of cosmological parameters within our emulation bounds set in Table 2. We show the result of comparing one model with `Pybird` (baseline - dashed black), `CLASS-PT` (dotted red) and `Sym-EFT` (solid blue) in the top panel of Fig 8. The linear P_{11} is shown as a guideline (green dot-dashed). We see that our `Sym-EFT` emulator is closer to `Pybird` than is `CLASS-PT` and all three are within 0.5% of each other. Hence, our 0.5% error threshold is within current deviations between codes and thus sufficient. In the bottom panel of Fig 8, we show a comparison between `Sym-EFT` and `Pybird` for 1000 cosmologies sampled from a Latin hypercube within the same bounds as in Table.2. Our comparison shows excellent agreement within 0.5% for 1σ, and barely over for 2σ. The dip around the lowest displayed
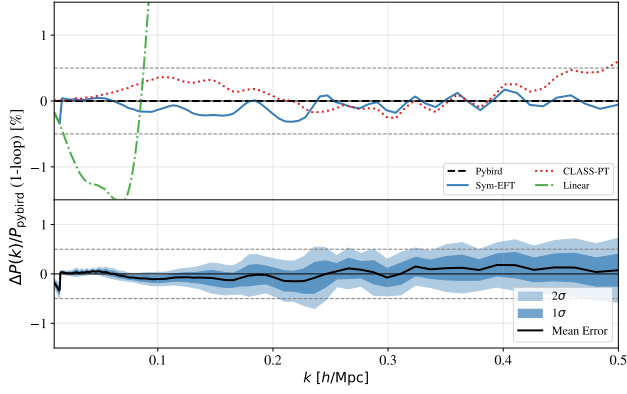
Figure 8. *Top:* IR-resummed $P^{\mathrm{SPT}}_{1-\mathrm{loop}}(k)$ %-relative difference of `Sym-EFT` (solid blue), `CLASS-PT` (dotted red), and linear (dashed green) compare respectively with `Pybird`. *Bottom:* IR-resummed $P^{\mathrm{SPT}}_{1-\mathrm{loop}}(k)$ mean error (black), 1σ and 2σ % error for 1000 cosmologies, relative to `Pybird`.

	One-loop (sec)	Two-loop (sec)
CosmoEFT+ResumEFT	15.56	965.78
Pybird	3.15	-
CLASS-PT	1.46	-
Sym-EFT	1.3×10^{-4}	3.5×10^{-4}

Table 4. Running times for one and two loops of EFTofLSS codes. The `CosmoEFT` used 8 cores, while `Sym-EFT` only one. The reported running times of `Pybird` and `CLASS-PT` differ from those reported in their respective articles by a factor of a few, the reason being likely to be compiler optimization flags. Changing those would also affect the running time of `Sym-EFT`.

k-values in both panels is due to our joining of `Sym-EFT` to the linear spectrum for $k < 0.01h\mathrm{Mpc}^{-1}$ using an error function. Let us note that these timings do not include the computation of P_{11}, for all codes used. To keep the total computation time small, one can use an emulator for P_{11}, preferably the symbolic emulator of Bartlett et al. (2024b).

We finally compare the mean running time of these codes to perform the EFT computations. These are shown in Table 4. CosmoEFT does not have the efficiency of `Pybird` and `CLASS-PT`, however, `Sym-EFT` being based on pure function computations leads to $12000 - 24000$ speedup over the last two. At two loops we had only `CosmoEFT` to compare with, and the speedup increases to $\sim 2 \times 10^6$. We note that the `CosmoEFT` computation was done using OpenMP on eight CPU cores, while `Sym-EFT` used only one CPU core, hence, factoring this in, we have naive speedups around $\sim 10^6$ and $\sim 2 \times 10^7$ compared to `CosmoEFT` at 1- and 2-loops respectively.

3.4.1 Redshift dependence

We tested the accuracy of the redshift dependence of the 2-loop `Sym-EFT` emulator as it affects the CMB angular power spectra. Specifically, the EFTofLSS matter power spectrum affects the CMB anisotropies through the integral of the potential $\Phi(k, z)$ over a redshift-dependent kernel, see Lewis & Challinor (2006). Therefore any redshift variation of the EFTofLSS matter power spectrum will be directly translated to $C_\ell^{\Phi\Phi}$, and further into the (lensed) temperature C_ℓ^{TT}, and polarization angular power spectra. To do this properly it is necessary to make assumptions about the exact redshift dependence of the counterterms. We chose to parametrise the counterterms as the
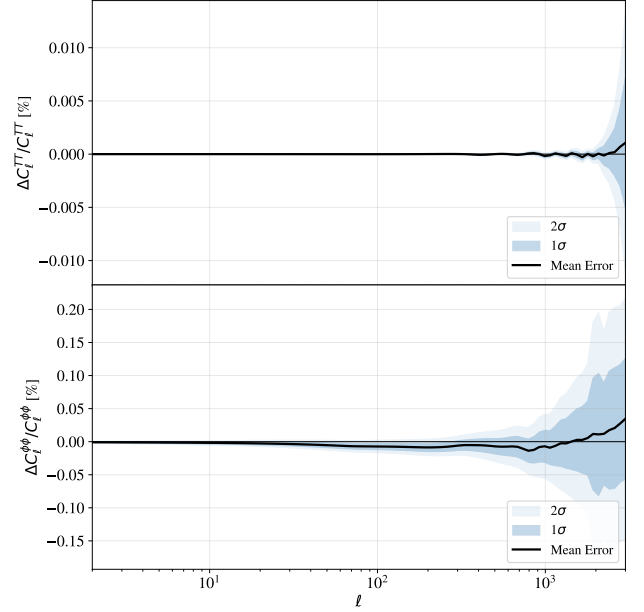

Figure 9. *Top:* The %-relative error of 2-loop `Sym-EFT` contrasted with `ResumEFT(CosmoEFT-Class)` as they contribute to the C_l^{TT} lensed temperature angular power spectrum for our 200 training set cosmologies. Shown is the mean error (solid blue), 1σ band (blue shade) and 2σ % band (light blue shade). *Bottom:* Same as the *top* panel, but for the $C_l^{\Phi\Phi}$ lensing potential angular power spectrum.

sum of two powerlaws of the growth factor, following the proposal of Foreman et al. (2015). Specifically, we set

$$c_{s(1)}(z) = A_{\mathrm{cs}}D(z)^{\alpha_s} + B_{\mathrm{cs}}D(z)^{\beta_s} \,,$$
$$c_1(z) = A_1 D(z)^{\alpha_1} + B_1 D(z)^{\beta_1} \,, \tag{21}$$
$$c_4(z) = A_4 D(z)^{\alpha_4} + B_4 D(z)^{\beta_4} \,,$$

with $A_{\mathrm{cs}} = 0.0130$, $B_{\mathrm{cs}} = 0.0220$, $a_{\mathrm{cs}} = 8.9958$, $b_{\mathrm{cs}} = -0.3957$, $A_1 = -0.1059$, $B_1 = 0.7644$, $a_1 = 0.5513$, $b_1 = 1.2506$, $A_4 = 0.1061$, $B_4 = 0.0824$, $a_4 = 2.5413$, $b_4 = 4.7726$. We have further set $c_{s(2)} = 0$, as Foreman et al. (2015) justified that this particular counterterm is very small and letting it vanish is a good approximation.

We note that our chosen values for the parameters in (21) are different from those in Foreman et al. (2015), as we fitted the counterterms to the `Syren-New` matter power spectrum and to the resulting $C_\ell^{\Phi\Phi}$ up to $\ell = 1500$, taking into account a redshift dependent k_{fail} (Calderon et al. 2025). In Fig.9 we show the error between `CosmoEFT-Class` and `Sym-EFT` for the 200 cosmologies in our training set, keeping the counterterms fixed as in (21). We find excellent agreement within 0.01% at 2σ for C_ℓ^{TT} (top panel) up to $\ell = 2500$, and within 0.05% at 2σ for $C_\ell^{\Phi\Phi}$ (bottom panel) up to $\ell = 1000$.

4 DISCUSSION AND CONCLUSION

We have presented an emulator suite for the EFTofLSS dark matter one- and two-loop power spectrum using the technique of symbolic regression. The emulator suite consists of ten emulators for the different terms that appear in the EFTofLSS power spectra, see (14) and (16), Three of these emulators were split in smaller overlapping regions in k space, see Section 3.3.1 and 3.3.2, as well as Table.3. Our

emulators are pure fitting functions which depend on k and the cosmological parameters, that can be inserted into any computer code, leading to $\sim 10^{-4} sec$ per model computation time; see (17), (19) and appendices A and B. This method provides the fastest possible emulation technique. We have chosen as simple expressions as allowed to keep within a threshold of $\sim 0.5\%$ which in the case of 1-loop is comparable with the current differences between EFTofLSS codes.

Apart from their use in ultra-fast MCMC based testing of ΛCDM with data in the mildly non-linear regime, one direct application is to use them in addition with CMB data. It has been shown that the CMB lensing is sensitive to larger scales than the galaxy lensing surveys, and has a wider redshift range Doux & Karwal (2025). Thus, we expect to see the complementary effect of two-loop EFTofLSS in the CMB lensing at different redshift and k ranges than cosmic shear.

While we targeted an emulation error of $\sim 0.5\%$, we are confident that our symbolic regression technique can reach better accuracy sacrifysing neither model length nor computational time. Given that current one-loop codes exhibit differences comparable with this error threshold, it seems that the current bottleneck is the accuracy of single un-emulated models. It would thus be interesting to have a global comparison between all codes in order to reach sub-0.1% accuracy.

While this work was in its final stages, there have been two other articles on accelerating the two-loop EFTofLSS matter power spectrum, (Bakx et al. 2025) and (Anastasiou et al. 2025). These two articles use different techniques and would be interesting to compare their output in a similar way as we have discussed above.

ACKNOWLEDGEMENTS

DATA AVAILABILITY

The raw power spectra of the cosmologies used in training and validating our emulators, as well as, all the emulator functions in C and python will be made publicly available after publication.

REFERENCES

Abbott T. M. C., et al., 2025, 2503.13632
Abdalla E., et al., 2022, JHEAp, 34, 49
Abdul Karim M., et al., 2025
Ade P., et al., 2019, JCAP, 02, 056
Aghanim N., et al., 2020, Astron. Astrophys., 641, A6
Anastasiou C., Favorito A., Lewandowski M., Senatore L., Zheng H., 2025
Angulo R. E., Zennaro M., Contreras S., Aricò G., Pellejero-Ibañez M., Stücker J., 2021, Mon. Not. Roy. Astron. Soc., 507, 5869
Aricò G., Angulo R. E., Contreras S., Ondaro-Mallea L., Pellejero-Ibañez M., Zennaro M., 2021, Mon. Not. Roy. Astron. Soc., 506, 4070
Bakx T., Rubira H., Chisari N. E., Vlah Z., 2025, Rapid cosmological inference with the two-loop matter power spectrum (arXiv:2508.00611), https://arxiv.org/abs/2508.00611
Bardeen J. M., Bond J. R., Kaiser N., Szalay A. S., 1986, Astrophys. J., 304, 15
Bartlett D. J., Pandey S., 2025, Symbolic Emulators for Cosmology: Accelerating Cosmological Analyses Without Sacrificing Precision (arXiv:2510.18749), https://arxiv.org/abs/2510.18749
Bartlett D. J., Wandelt B. D., Zennaro M., Ferreira P. G., Desmond H., 2024a, Astron. Astrophys., 686, A150
Bartlett D. J., et al., 2024b, Astron. Astrophys., 686, A209
Baumann D., Nicolis A., Senatore L., Zaldarriaga M., 2012, JCAP, 07, 051
Bennett C. L., et al., 2013, Astrophys. J. Suppl., 208, 20
Bernardeau F., Colombi S., Gaztanaga E., Scoccimarro R., 2002, Phys. Rept., 367, 1
Blas D., Lesgourgues J., Tram T., 2011, Journal of Cosmology and Astroparticle Physics, 2011, 034–034
Bond J. R., Efstathiou G., 1984, Astrophys. J. Lett., 285, L45
Brout D., et al., 2022, Astrophys. J., 938, 111
Burlacu B., Kronberger G., Kommenda M., 2020, in Proceedings of the 2020 Genetic and Evolutionary Computation Conference Companion. GECCO '20. Association for Computing Machinery, New York, NY, USA, p. 1562–1570, doi:10.1145/3377929.3398099, https://doi.org/10.1145/3377929.3398099
Calderon R., Farakou D., Skordis C., 2025, In preparation
Camphuis E., et al., 2025
Carlson J., White M., Padmanabhan N., 2009, Physical Review D, 80
Carrasco J. J. M., Hertzberg M. P., Senatore L., 2012, JHEP, 09, 082
Carrasco J. J. M., Foreman S., Green D., Senatore L., 2014a, JCAP, 07, 056
Carrasco J. J. M., Foreman S., Green D., Senatore L., 2014b, JCAP, 07, 057
Cataneo M., Foreman S., Senatore L., 2017, JCAP, 04, 026
Cava W. G. L., Orzechowski P., Burlacu B., de França F. O., Virgolin M., Jin Y., Kommenda M., Moore J. H., 2021, CoRR, abs/2107.14351
Chapman M. J., et al., 2022, Mon. Not. Roy. Astron. Soc., 516, 617
Chudaykin A., Ivanov M. M., Philcox O. H. E., Simonović M., 2020, Phys. Rev. D, 102, 063533
D'Amico G., Senatore L., Zhang P., 2021, JCAP, 01, 006
Dodelson S., Schmidt F., 2020, Modern Cosmology, 2nd edition edn. Academic Press
Doux C., Karwal T., 2025, Going beyond S_8: fast inference of the matter power spectrum from weak-lensing surveys (arXiv:2506.16434), https://arxiv.org/abs/2506.16434
Eifler T., et al., 2021, Mon. Not. Roy. Astron. Soc., 507, 1746
Eisenstein D. J., Hu W., 1998, Astrophys. J., 496, 605
Foreman S., Perrier H., Senatore L., 2015,] 10.1088/1475-7516/2016/05/027
Garcia-Quintero C., et al., 2025
Ge F., et al., 2024, arXiv e-prints, p. arXiv:2411.06000
Gebhardt K., et al., 2021, Astrophys. J., 923, 217
Giblin B., Cataneo M., Moews B., Heymans C., 2019, Mon. Not. Roy. Astron. Soc., 490, 4826
Goroff M. H., Grinstein B., Rey S. J., Wise M. B., 1986, Astrophys. J., 311, 6
Hahn T., 2005, Comput. Phys. Commun., 168, 78
Heitmann K., Higdon D., Nakhleh C., Habib S., 2006, Astrophys. J. Lett., 646, L1
Heitmann K., Higdon D., White M., Habib S., Williams B. J., Wagner C., 2009, Astrophys. J., 705, 156
Heitmann K., Lawrence E., Kwan J., Habib S., Higdon D., 2014, Astrophys. J., 780, 111
Hertzberg M. P., 2014, Phys. Rev. D, 89, 043521
Jain B., Bertschinger E., 1994, Astrophys. J., 431, 495
Kammerer L., Bartlett D. J., Kronberger G., Desmond H., Ferreira P. G., 2025, Astron. Astrophys., 701, A284
Knabenhans M., et al., 2021, Mon. Not. Roy. Astron. Soc., 505, 2840

Koza J. R., 1992, Genetic programming. On the programming of computers by means of natural selection

Kronberger G., Olivetti de Franca F., Desmond H., Bartlett D. J., Kammerer L., 2024, in Affenzeller M., Winkler S. M., Kononova A. V., Trautmann H., Tušar T., Machado P., Bäck T., eds, Parallel Problem Solving from Nature – PPSN XVIII. Springer Nature Switzerland, Cham, pp 273–289 (arXiv:2404.17292)

Lewandowski M., Perko A., Senatore L., 2015, JCAP, 05, 019

Lewis A., Challinor A., 2006, Weak Gravitational Lensing of the CMB, http://cosmologist.info

Linde D., Moradinezhad Dizgah A., Radermacher C., Casas S., Lesgourgues J., 2024, JCAP, 07, 068

Lodha K., et al., 2025

Louis T., et al., 2025b, The Atacama Cosmology Telescope: DR6 Power Spectra, Likelihoods and ΛCDM Parameters (arXiv:2503.14452), https://arxiv.org/abs/2503.14452

Louis T., et al., 2025a

Mandelbaum R., et al., 2018

McClintock T., et al., 2019a

McClintock T., et al., 2019b, Astrophys. J., 872, 53

McQuinn M., White M., 2016, JCAP, 01, 043

Mellier Y., et al., 2025, Astron. Astrophys., 697, A1

Nishimichi T., et al., 2019, Astrophys. J., 884, 29

Pajer E., Zaldarriaga M., 2013, JCAP, 08, 037

Peacock J. A., Dodds S. J., 1994, Mon. Not. Roy. Astron. Soc., 267, 1020

Radwan Y. A., Kronberger G., Winkler S., 2024, arXiv e-prints, p. arXiv:2406.03585

Rubin D., et al., 2023

Sáez-Casares I., Rasera Y., Li B., 2024, Mon. Not. Roy. Astron. Soc., 527, 7242

Schneider A., et al., 2016, JCAP, 04, 047

Scolnic D. M., et al., 2018, Astrophys. J., 859, 101

Senatore L., 2018, Gravity@Prague 2018 Summer School (https://gravity-prague.fzu.cz/2018) – Lecture notes.

Senatore L., Zaldarriaga M., 2015, JCAP, 02, 013

Senatore L., Zaldarriaga M., 2017

Spurio Mancini A., Piras D., Alsing J., Joachimi B., Hobson M. P., 2021

Sui C., Bartlett D. J., Pandey S., Desmond H., Ferreira P. G., Wandelt B. D., 2025, Astron. Astrophys., 698, A1

Virgolin M., Pissis S. P., 2022, Transactions on Machine Learning Research

Winther H., Casas S., Baldi M., Koyama K., Li B., Lombriser L., Zhao G.-B., 2019, Phys. Rev. D, 100, 123540

Wright A. H., et al., 2025

Zhai Z., et al., 2019, Astrophys. J., 874, 95

Zhao G.-B., et al., 2021, Mon. Not. Roy. Astron. Soc., 504, 33
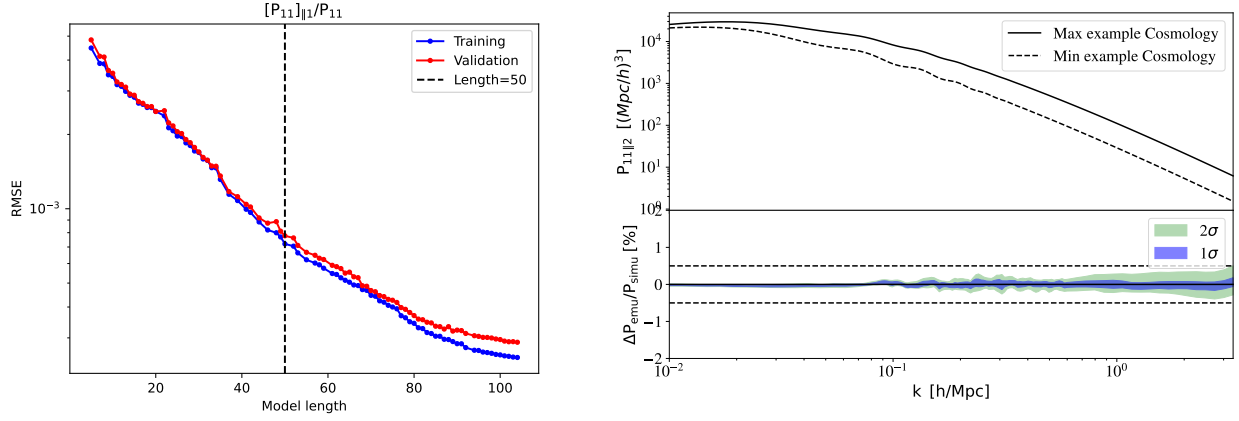
Zhao C., et al., 2024

Figure A1. *Left:* The Pareto front of RMSE vs model length for the $\frac{[P_{11}]_{\|1}}{P_{11}}$ emulator runs as generated by `Operon`, with blue marking the training and red the validation error, and with the chosen model of length 50 indicated by the vertical line. *Right:* The top plot shows the $[P_{11}]_{\|1}$ function for two extreme cases of cosmological parameters while the bottom plot displays the resulting 1σ and 2σ emulator % error for all 300 cosmologies. The horizontal dashed lines mark the 0.5% threshold.

APPENDIX A: THE 1-LOOP EMULATORS

At 1-loop the emulators concern the functions $[k^2 P_{11}(k)]_{\|0}$, $[P_{11}(k)]_{\|1}$ and $[P_{1-\text{loop}}(k)]_{\|0}$. The $[k^2 P_{11}(k)]_{\|0}$ has been presented in the main part of the article, see (17) and (18) as well as Fig.4 for the Pareto front and error plot respectively. Here we present the remaining two emulators.

A1 The $[P_{11}]_{\|1}$ emulator

For the $[P_{11}]_{\|1}$ emulator we chose a model of length 50. We show the Pareto front of RMSE vs model length on the left of Fig.A1. The form of the emulated function is

$$
\begin{aligned}
\frac{[P_{11}]_{\|1}}{P_{11}} =& C_{21} + k \left(C_0 \tilde{A}_s - C_1 k \right) \left(C_2 \tilde{A}_s \, (C_3 h)^{C_4 \Omega_{cb}} - C_5 \Omega_b \right) \cos\left(C_6 \Omega_{cb} + \frac{C_9}{\sqrt{C_{10} k^2 + 1}} + (C_7 h)^{C_8 \Omega_b} \right) \\
&+ \frac{\left(C_{11} \tilde{A}_s - \cos(C_{12} k) \right) \left(C_{13} \Omega_{cb} - C_{14} \Omega_b \right) \cos\left(C_{15} k \, (C_{16} h)^{C_{17} \Omega_{cb} + C_{18} \Omega_b} \right)}{\sqrt{(C_{19} \Omega_b - C_{20} k)^2 + 1}}
\end{aligned}
\tag{A1}
$$

where

$C_0 = 0.859$	$C_1 = 0.2675$	$C_2 = 4.03 \times 10^{-3}$	$C_3 = 2.096$	$C_4 = 5.96$	$C_5 = 0.192$
$C_6 = 5.3$	$C_7 = 1.2624$	$C_8 = 145.7$	$C_9 = 6.81$	$C_{10} = 121.6$	$C_{11} = 0.42$
$C_{12} = 9.73$	$C_{13} = 0.0117$	$C_{14} = 0.1624$	$C_{15} = 138.55$	$C_{16} = 0.26537$	$C_{17} = 0.46944$
$C_{18} = 1.487$	$C_{19} = 47.8$	$C_{20} = 11.62$	$C_{21} = 0.999883.$		

(A2)

The resulting error is displayed on the right of Fig.A1.

A2 The $[P_{1-\text{loop}}]_{\|0}$ emulator

The IR resummed $[P_{1-\text{loop}}]_{\|0}$ emulator is split into three regions in k space as described in Section 3.3.1, while all the Pareto fronts can be found in Fig.A2
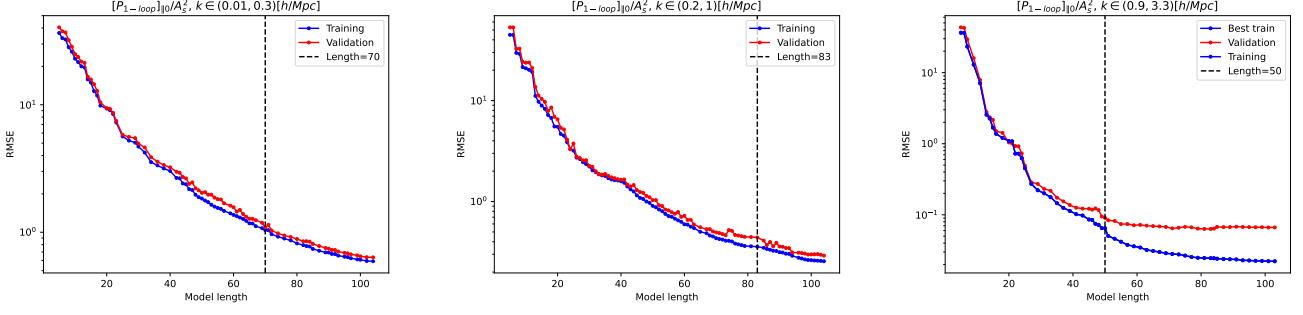
Figure A2. The Pareto fronts of RMSE vs model length for the three emulators of $\frac{[P_{1-\text{loop}}]_{\|0}}{\tilde{A}_s^2}$ runs as generated by `Operon`, with blue marking the training and red the validation error, and with the chosen models indicated by the vertical line.

A2.1 Region 1: $k = [0.01, 0.3] \times h\text{Mpc}^{-1}$

For the first region of the $[P_{1-\text{loop}}]_{\|0}$ emulator we chose a model of length 70, see left panel of Fig.A2. The resulting function is

$$
\begin{aligned}
\frac{[P_{1-\text{loop}}]_{\|0}^{(1)}}{\tilde{A}_s^2} = &-C_0 h\, (C_1 h)^{C_2 \Omega_b} \cos\left(\frac{C_3 h + C_4 k}{\sqrt{(C_5 \Omega_{cb} + C_6 \Omega_b)^2 + 1}}\right) \cos\left(C_7 \Omega_{cb} + \frac{C_8}{\sqrt{C_9 k^2 + 1}}\right) - C_{30} \\
&- \frac{n_s\,(C_{10}\Omega_{cb} - C_{11}\Omega_b)\ln(C_{12}k)^{C_{13} + \frac{C_{14}\Omega_{cb} - C_{15}\Omega_b}{\sqrt{(C_{16}n_s)^{-C_{17}\Omega_{cb}} + 1}}} \cos\left(\frac{C_{18}\Omega_{cb}\cos(C_{19}n_s)}{\sqrt{C_{20}k^2 + 1}} - C_{21}h - \frac{C_{22}n_s}{\sqrt{\frac{(C_{23}\Omega_{cb} + C_{24}k)^2}{(C_{25}\Omega_{cb} - C_{26}\Omega_b)^2 + 1}} + 1}\right)}{\sqrt{(C_{27}h)^{-C_{28}n_s} + 1}\sqrt{C_{29}\Omega_{cb}^2 + 1}}
\end{aligned}
\tag{A3}
$$

where

$C_0 = 12.9$	$C_1 = 2.355$	$C_2 = 28$	$C_3 = 3.89$	$C_4 = 122.62$	$C_5 = 1.5224$
$C_6 = 4.764$	$C_7 = 1.656$	$C_8 = 4.363$	$C_9 = 188.7$	$C_{10} = 859.4$	$C_{11} = 1714$
$C_{12} = 203.3$	$C_{13} = 0.9403$	$C_{14} = 7.62$	$C_{15} = 15.26$	$C_{16} = 0.555$	$C_{17} = 4.973$
$C_{18} = 3.7$	$C_{19} = 4.742$	$C_{20} = 4200$	$C_{21} = 2.028$	$C_{22} = 50.37$	$C_{23} = 202.44$
$C_{24} = 574.8$	$C_{25} = 27.634$	$C_{26} = 23.39$	$C_{27} = 0.84518$	$C_{28} = 6.498$	$C_{29} = 13.745$
$C_{30} = 0.01$					(A4)

A2.2 Region 2: $k = [0.2, 1] \times h\text{Mpc}^{-1}$

For the second region of the $[P_{1-\text{loop}}]_{\|0}$ emulator we chose a model of length 83, see the middle panel of Fig.A2. The resulting function will be supplied after publication.

A2.3 Region 3: $k = [0.9, 3.3] \times h\text{Mpc}^{-1}$

For the third region of the $[P_{1-\text{loop}}]_{\|0}$ emulator we chose a model of length 50, see the right panel of Fig.A2. The resulting function is

$$
\begin{aligned}
\frac{[P_{1-\text{loop}}]_{\|0}^{(3)}}{\tilde{A}_s^2} = &(C_0 k)^{C_1 \tilde{A}_s + C_2 n_s - C_3} (C_4 h)^{-C_5 \Omega_b + C_6 n_s + C_7} (C_9 + C_8 \Omega_{cb})^{\frac{C_{11}\Omega_b + C_{12}h}{\sqrt{C_{13}\Omega_{cb}^2 + 1}} + \ln(C_{10}k)} \\
&\times \left(-C_{14}k + \ln(C_{15}h) + \frac{C_{16}\Omega_{cb} + C_{17}\Omega_b - \frac{1}{(C_{18}k)^{C_{19}\Omega_{cb}\ln(C_{20}h)}}}{\sqrt{C_{21}k^2 + 1}}\right) - C_{22}
\end{aligned}
\tag{A5}
$$

where

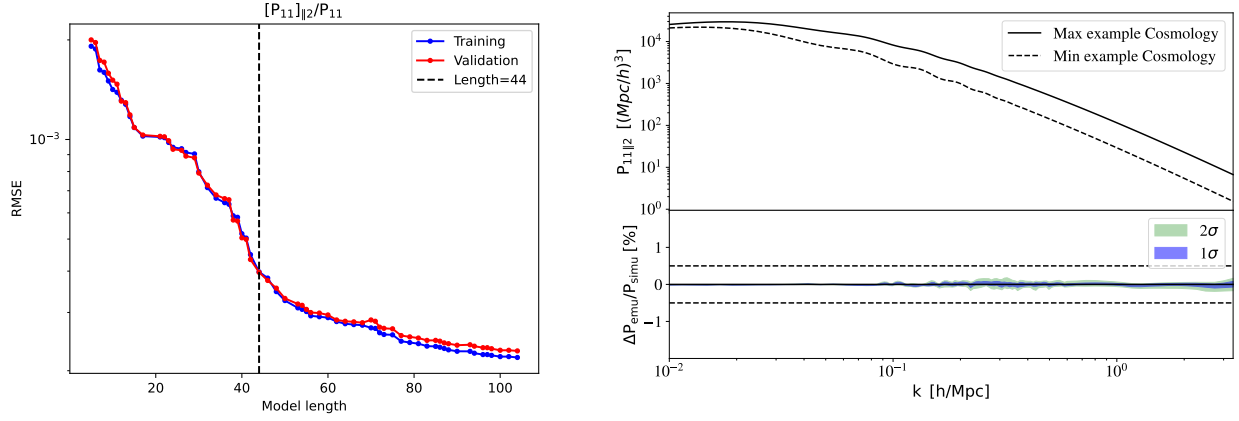|					
$C_0 = 1.1086$	$C_1 = 0.0154$	$C_2 = 1.9261$	$C_3 = 1.21245$	$C_4 = 7.07172$	$C_5 = 6.339$
$C_6 = 1.91047$	$C_7 = 3.85764$	$C_8 = 0.3437$	$C_9 = 0.041539$	$C_{10} = 3.216055$	$C_{11} = 57.033$
$C_{12} = 1.668$	$C_{13} = 171.47$	$C_{14} = 0.043$	$C_{15} = 2.8331$	$C_{16} = 4.8072$	$C_{17} = 8.635$
$C_{18} = 0.3023$	$C_{19} = 1.2287$	$C_{20} = 3.4138$	$C_{21} = 0.4648$	$C_{22} = 8 \times 10^{-4}$	(A6)

Figure B1. Left: The Pareto front of RMSE vs model length for the $\frac{[P_{11}]_{\|2}}{P_{11}}$ emulator runs as generated by `Operon`, with blue marking the training and red the validation error, and with the chosen model of length 44 indicated by the vertical line. **Right:** The top plot shows the $[P_{11}]_{\|2}$ function for two extreme cases of cosmological parameters while the bottom plot displays the resulting 1σ and 2σ emulator % error for all 300 cosmologies.

APPENDIX B: THE 2-LOOP EMULATORS

At 2-loop, the emulators concern the functions $[P_{11}(k)]_{\|2}$, $[k^2 P_{11}(k)]_{\|1}$, $[k^4 P_{11}(k)]_{\|0}$, $[P_{1-\text{loop}}(k)]_{\|1}$, $[P_{2-\text{loop}}(k)]_{\|0}$, $[P_{1-\text{loop}}^{(\text{cs})}]_{\|0}$ and $[P_{1-\text{loop}}^{(\text{quad})}]_{\|0}$. The $[k^2 P_{11}(k)]_{\|1}$ has been presented in the main part of the article, see (17) and (20) as well as Fig.6 for the Pareto front and error plot. Here we present the remaining emulators.

B1 The $[P_{11}]_{\|2}$ emulator

For the $[P_{11}]_{\|2}$ emulator we chose a model of length 44 in order to be within our P_{2-loop}^{SPT} error threshold. We show the Pareto front of RMSE vs model length on the left of Fig.B1. The form of the emulated function is

$$\frac{[P_{11}]_{\|2}}{P_{11}} = C_{21} - \frac{(C_0 h)^{C_1 \tilde{A}_s} (C_2 \Omega_{cb} - C_3 \Omega_b) \left(C_4 n_s - (C_5 k)^{C_6 \Omega_{cb}}\right)}{\sqrt{(C_7 k)^{-C_8 \Omega_{cb}} + 1}} - \frac{1}{\sqrt{(C_{19} k)^{C_{20} \tilde{A}_s} + 1}} \left[\frac{C_{10} \cos\left(\frac{C_{11} h + C_{12} k}{\sqrt{(C_{13} \Omega_{cb} + C_{14} \Omega_b)^2 + 1}}\right)}{\sqrt{\left(C_{15} \Omega_b - C_{16} k - (C_{17} k)^{-C_{18} n_s}\right)^2 + 1}} + C_9 \right]$$

(B1)

where

$C_0 = 2.746$	$C_1 = 2.343$	$C_2 = 7.63 \times 10^{-3}$	$C_3 = 0.0265$	$C_4 = 0.711$	$C_5 = 0.408$
$C_6 = 0.8$	$C_7 = 1.78$	$C_8 = 13.6$	$C_9 = 5.525 \times 10^{-3}$	$C_{10} = 0.01016$	$C_{11} = 11.5$
$C_{12} = 113.84$	$C_{13} = 1.41$	$C_{14} = 4.63$	$C_{15} = 154.6$	$C_{16} = 25.97$	$C_{17} = 2.444$
$C_{18} = 4.067$	$C_{19} = 2.51$	$C_{20} = 3.48$	$C_{21} = 1.005462$		

(B2)

The resulting error is displayed on the right of Fig.B1.

B2 The $[k^4 P_{11}]_{\|0}$ emulator

For the $[k^4 P_{11}]_{\|0}$ emulator we chose a model of length 70 in order to be within our P_{2-loop}^{SPT} error threshold. We show the Pareto front of RMSE vs model length on the left of Fig.B2. The form of the emulated function is

$$\frac{[k^4 P_{11}]_{\|0}}{k^4 P_{11}} = C_0 \tilde{A}_s + C_1 \Omega_{cb} + C_{18} + \frac{C_2 (C_3 h)^{C_4 \Omega_{cb} - C_5 \Omega_b} \left(\frac{\tilde{A}_s}{C_{13} k}\right)^{C_{14} \Omega_{cb}}}{\sqrt{\left(C_{15} \Omega_{cb} - \frac{C_{16} k}{\sqrt{C_{17} k^2 + 1}}\right)^2 + 1}} \left(-C_6 \Omega_{cb} + C_7 n_s + \frac{C_{10} k + C_9 \Omega_b}{\sqrt{(C_{11} k)^{-C_{12} k} + 1}} + \cos(C_8 k)\right)$$

$$+ \frac{(-C_{19} \tilde{A}_s + C_{20} \Omega_{cb} - C_{21} \Omega_b + C_{22} \cos(C_{23} k)) \cos\left(\frac{C_{24} h + C_{25} k}{\sqrt{(C_{26} \Omega_{cb} + C_{27} \Omega_b)^2 + 1}}\right)}{\sqrt{(C_{28} \Omega_b - C_{29} k)^2 + 1}} + \frac{-C_{30} n_s + C_{31} k + C_{32}}{\sqrt{C_{33} k^2 + 1}}$$
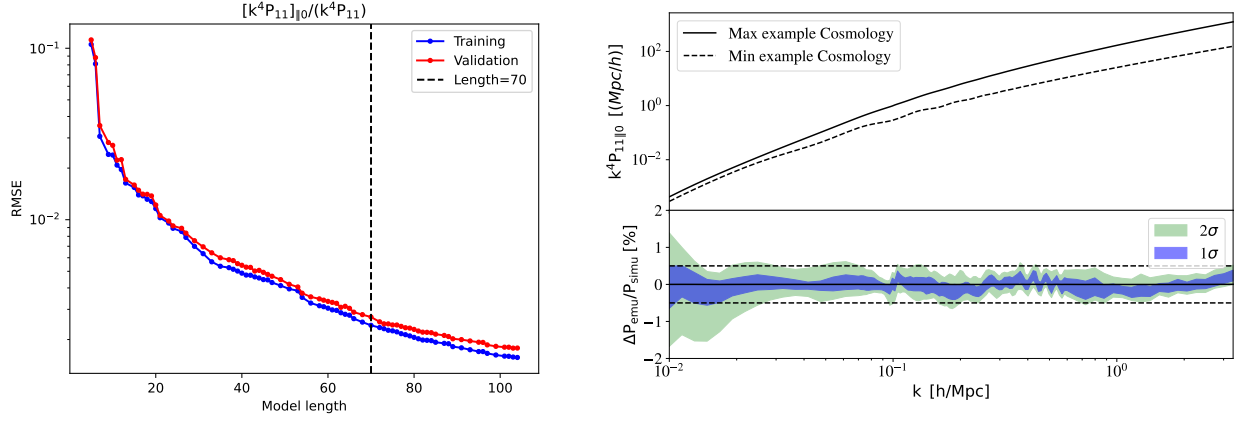
(B3)

Figure B2. Left: The Pareto front of RMSE vs model length for the $\frac{[k^4 P_{11}]_{\|0}}{k^4 P_{11}}$ emulator runs as generated by `Operon`, with blue marking the training and red the validation error, and with the chosen model of length 70 indicated by the vertical line. **Right:** The top plot shows the $[k^4 P_{11}]_{\|0}$ function for two extreme cases of cosmological parameters while the bottom plot displays the resulting 1σ and 2σ emulator % error for all 300 cosmologies.
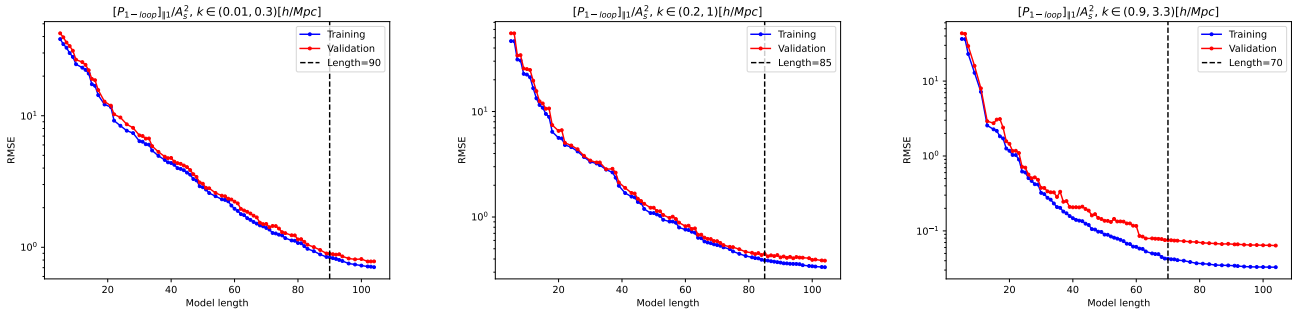

Figure B3. The Pareto fronts of RMSE vs model length for the three emulators of $\frac{[P_{1-\text{loop}}]_{\|1}}{\bar{A}_s^2}$ runs as generated by `Operon`, with blue marking the training and red the validation error, and with the chosen models indicated by the vertical line.

where

$C_0 = 3.84 \times 10^{-3}$	$C_1 = 0.2188$	$C_2 = 0.01$	$C_3 = 5.586$	$C_4 = 6.923$	$C_5 = 8.222$
$C_6 = 34.7$	$C_7 = 38.75$	$C_8 = 117.27$	$C_9 = 127$	$C_{10} = 18.87$	$C_{11} = 9.85$
$C_{12} = 2000$	$C_{13} = 1297$	$C_{14} = 1.8743$	$C_{15} = 2.7745$	$C_{16} = 107.9$	$C_{17} = 613$
$C_{18} = 2 \times 10^{-5}$	$C_{19} = 7.02 \times 10^{-3}$	$C_{20} = 0.074$	$C_{21} = 0.472$	$C_{22} = 0.01$	$C_{23} = 12.12$
$C_{24} = 9.866$	$C_{25} = 116.5$	$C_{26} = 1.352$	$C_{27} = 4.704$	$C_{28} = 43.1$	$C_{29} = 14.4$
$C_{30} = 0.3267$	$C_{31} = 50.062$	$C_{32} = 0.455$	$C_{33} = 3187.7$		(B4)

The resulting error is displayed on the right of Fig.B2

B3 The $[P_{1-\text{loop}}]_{\|1}$ emulator

The IR resummed $[P_{1-\text{loop}}]_{\|1}$ emulator is split into three regions in k space as described in Section 3.3.2, while all the Pareto fronts can be found in Fig.B3

B3.1 Region 1: $k = [0.01, 0.3] \times h\text{Mpc}^{-1}$

For the first region of the $[P_{1-\text{loop}}]_{\parallel 1}$ emulator we chose a model of length 70, see left panel of Fig.B3. The resulting function is

$$
\frac{[P_{1-\text{loop}}]_{\parallel 1}^{(1)}}{\tilde{A}_s^2} = -C_0 + \frac{\left[\left(\frac{C_1 k}{\sqrt{C_2 k^2+1}}\right)^{C_3 \Omega_{cb}} - \cos(C_4 n_s - \ln(C_5 k))\right]\left[C_8 \Omega_b - \Omega_{cb}(C_6 h - C_7 n_s) - \cos\left(C_9 h - \frac{C_{10} k}{\sqrt{C_{11}\Omega_{cb}^2+1}}\right)\right]}{\sqrt{(C_{35}k)^{-C_{36}\Omega_{cb}+\frac{C_{37}k}{\sqrt{C_{38}k^2+1}}} + 1}} \left\{ -C_{12}\Omega_{cb} \right.
$$
$$
+ C_{13}k + (C_{14}h)^{C_{15}-C_{16}\Omega_b}(-C_{17}\Omega_b + \Omega_{cb})[-C_{20}\Omega_{cb} - C_{21}k + \Omega_{cb}(C_{18}h + C_{19}n_s)] + (C_{33}k)^{-C_{34}\Omega_{cb}}
$$
$$
+ \cos\left(-C_{22}\Omega_b + C_{23}h + \frac{C_{24}k}{\sqrt{C_{25}\Omega_{cb}^2+1}}\right) + \cos\left(C_{26}\Omega_b + C_{27}h + \frac{C_{28}k}{\sqrt{(C_{29}\Omega_{cb}+C_{30}\Omega_b)^2+1}} + \frac{C_{31}k}{\sqrt{C_{32}k^2+1}}\right)\right\} \tag{B5}
$$

where

$C_0 = 0.01$	$C_1 = 5.672$	$C_2 = 23.847$	$C_3 = 4.378$	$C_4 = 0.81636$	$C_5 = 3.336$
$C_6 = 430.88$	$C_7 = 127.53$	$C_8 = 276.55$	$C_9 = 2.643$	$C_{10} = 119.07$	$C_{11} = 3.461$
$C_{12} = 38.113$	$C_{13} = 23.725$	$C_{14} = 3.22496$	$C_{15} = 2.8447$	$C_{16} = 10.353$	$C_{17} = 2.1854$
$C_{18} = 7.224$	$C_{19} = 49.34$	$C_{20} = 21.03$	$C_{21} = 75.24$	$C_{22} = 56.83$	$C_{23} = 3.291$
$C_{24} = 116.47$	$C_{25} = 3.245$	$C_{26} = 27.45$	$C_{27} = 3.66$	$C_{28} = 120.39$	$C_{29} = 1.834$
$C_{30} = 5.294$	$C_{31} = 22.9$	$C_{32} = 96$	$C_{33} = 2.922$	$C_{34} = 3.816$	$C_{35} = 5.834$
$C_{36} = 12.544$	$C_{37} = 31.5$	$C_{38} = 465$			

$$\tag{B6}$$

B3.2 Region 2: $k = [0.2, 1] \times h\text{Mpc}^{-1}$

For the second region of the $[P_{1-\text{loop}}]_{\parallel 1}$ emulator we chose a model of length 83, see the middle panel of Fig.B3. The resulting function will be supplied after publication.

B3.3 Region 3: $k = [0.9, 3.3] \times h\text{Mpc}^{-1}$

For the third region of the $[P_{1-\text{loop}}]_{\parallel 1}$ emulator we chose a model of length 50, see the right panel of Fig.B3. The resulting function is

$$
\frac{[P_{1-\text{loop}}]_{\parallel 1}^{(3)}}{\tilde{A}_s^2} = \frac{C_0 (C_1 n_s)^{C_2 k + C_3}(C_4 h - 1)(C_5 \Omega_{cb} - C_6 \Omega_b - 1)(C_7 \Omega_{cb} - C_8 \Omega_b - k)\left(-C_{10}h - C_{11}n_s + C_9 \tilde{A}_s + (C_{12}h + C_{13}k)^{C_{14}k}\right)}{\sqrt{\left[1 + \frac{(C_{15}\Omega_{cb}+C_{16}k-\ln(C_{17}h))^2}{(C_{18}\Omega_{cb}-C_{19}\Omega_b+C_{20}h-C_{21})^2+1}\right](C_{22}k^2+1)\left[\left(C_{23}\Omega_b + (C_{24}h)^{-C_{25}h}\right)^2+1\right]}}
$$
$$
\times \frac{1}{\sqrt{\left(C_{26}h + C_{27}n_s - C_{28} - (C_{29}k)^{-C_{30}\Omega_{cb}}\right)^2 + 1}} + C_{31} \tag{B7}
$$

where

$C_0 = 4032.6$	$C_1 = 0.30666$	$C_2 = 0.38145$	$C_3 = 2.0405$	$C_4 = 2.7333$	$C_5 = 12.0496$
$C_6 = 14.467$	$C_7 = 80.831$	$C_8 = 129.8$	$C_9 = 1.1 \times 10^{-3}$	$C_{10} = 0.3266$	$C_{11} = 0.6959$
$C_{12} = 4.1534$	$C_{13} = 0.2649$	$C_{14} = 0.28992$	$C_{15} = 2.19$	$C_{16} = 2.9544$	$C_{17} = 3.225$
$C_{18} = 8.357$	$C_{19} = 15.81$	$C_{20} = 0.5555$	$C_{21} = 0.9718$	$C_{22} = 5.666$	$C_{23} = 25.673$
$C_{24} = 1.3491$	$C_{25} = 5.445$	$C_{26} = 3.6656$	$C_{27} = 5.7639$	$C_{28} = 9.1967$	$C_{29} = 0.841$
$C_{30} = 1.256$	$C_{31} = 3 \times 10^{-3}$				

$$\tag{B8}$$

B4 The $[P_{2-\text{loop}}]_{\parallel 0}$ emulator

The IR resummed $[P_{2-\text{loop}}]_{\parallel 0}$ emulator is split into two overlaping regions in k space as described in Section 3.3.2, while all the Pareto fronts can be found in Fig.B4
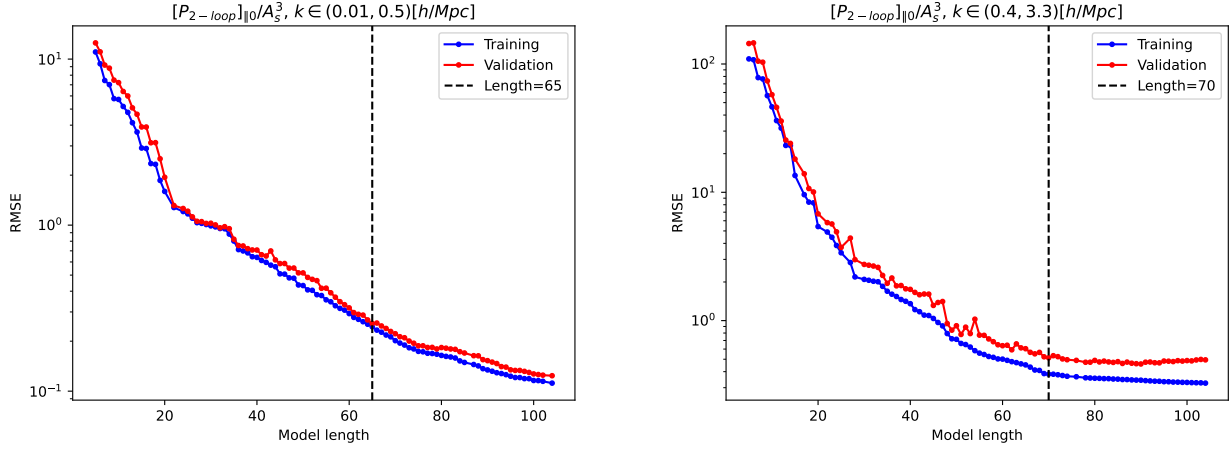
Figure B4. The Pareto fronts of RMSE vs model length for the three emulators of $\frac{[P_{2-loop}]_{\|0}}{\tilde{A}_s^3}$ runs as generated by `Operon`, with blue marking the training and red the validation error, and with the chosen models indicated by the vertical line.

B4.1 Region 1: $k = [0.01, 0.5] \times h\mathrm{Mpc}^{-1}$

For the first region of the $[P_{2-\mathrm{loop}}]_{\|0}$ emulator we chose a model of length 65, see the right panel of Fig.B4. The resulting function is

$$
\frac{[P_{2-\mathrm{loop}}]_{\|0}^{(1)}}{\tilde{A}_s^3} = \frac{(C_0 h)^{C_1\Omega_{cb} - \frac{C_2\Omega_{cb}}{\sqrt{C_3 k^2 + 1}} + C_4 n_s}}{\sqrt{(C_{27}k)^{-C_{28}n_s} + 1}} \left(\frac{C_5\Omega_{cb}}{\sqrt{C_6\Omega_b^2 + 1}} - \frac{1}{(C_7 k)^{C_8 k}} \right) \left[C_9 h \left(-C_{10}\Omega_b + \Omega_{cb} \right) \cos\left(\frac{(C_{11}h)^{C_{12}\Omega_{cb}} \left(-C_{13}\Omega_b + C_{14}n_s \right)}{\sqrt{\left(C_{15}\tilde{A}_s + C_{16}n_s + C_{17}k \right)^2 + 1}} \right) \right.
$$
$$
\left. - C_{18}k + C_{26} - (C_{19}k)^{C_{20}\Omega_b - C_{21}k} \cos\left(-C_{22}\Omega_b + C_{23}h + \frac{C_{24}k}{\sqrt{C_{25}\Omega_{cb}^2 + 1}} \right) \right] - C_{29}
\tag{B9}
$$

where

$C_0 = 3.867$	$C_1 = 2.187$	$C_2 = 8$	$C_3 = 146$	$C_4 = 5.023$	
$C_5 = 25.41$	$C_6 = 698$	$C_7 = 0.964$	$C_8 = 2.316$	$C_9 = 32.5$	$C_{10} = 1.588$
$C_{11} = 5.62$	$C_{12} = 1.394$	$C_{13} = 19.27$	$C_{14} = 8.556$	$C_{15} = 0.084$	$C_{16} = 1.542$
$C_{17} = 22.48$	$C_{18} = 7.585$	$C_{19} = 19$	$C_{20} = 23.5$	$C_{21} = 8.96$	$C_{22} = 38.4$
$C_{23} = 6.76$	$C_{24} = 113$	$C_{25} = 3.55$	$C_{26} = 2.451$	$C_{27} = 0.454$	$C_{28} = 3.365$
$C_{30} = 0.02$					$\tag{B10}$

B4.2 Region 2: $k = [0.4, 3.3] \times h\mathrm{Mpc}^{-1}$

For the second region of the $[P_{2-\mathrm{loop}}]_{\|0}$ emulator, we chose a model of length 70, see the right panel of Fig.B4 The resulting function will be supplied after publication.

B5 The $[P_{1-\mathrm{loop}}^{(\mathrm{cs})}]_{\|0}$ emulator

For the $[P_{1-\mathrm{loop}}^{(\mathrm{cs})}]_{\|0}$ emulator we chose a model of length 78. We show the Pareto front of RMSE vs model length on the left of Fig.B5. The form of the emulated function will be supplied after publication.
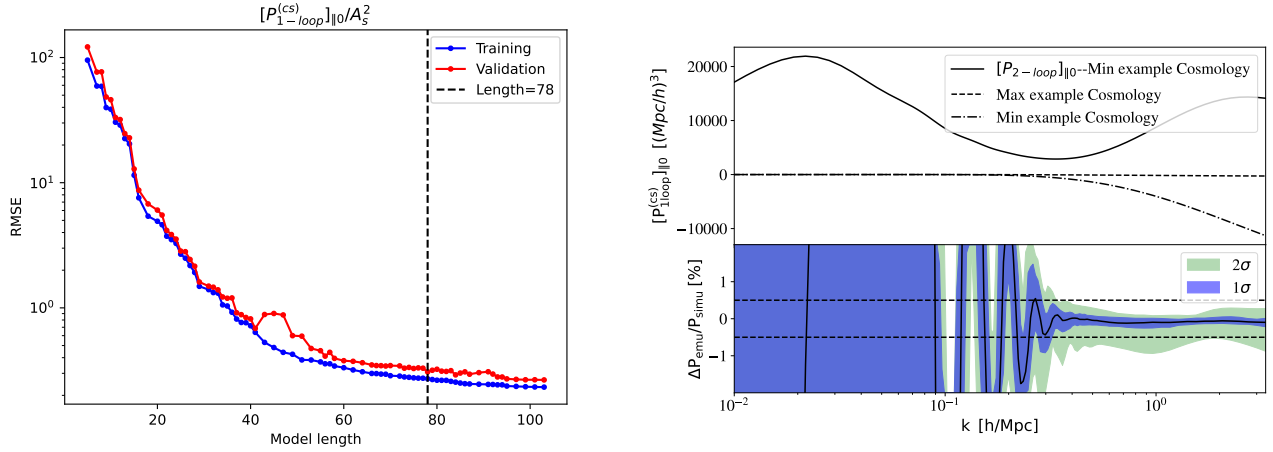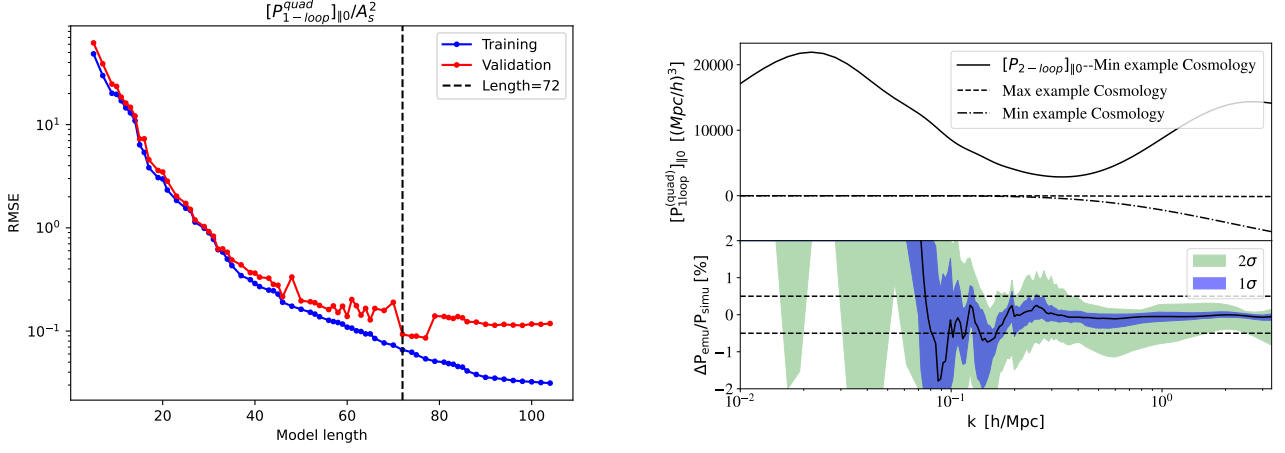
Figure B5. *Left:* The Pareto front of RMSE vs model length for the $\frac{[P^{(cs)}_{1loop}]_{\|0}}{\bar{A}_s^2}$ emulator runs as generated by Operon, with blue marking the training and red the validation error, and with the chosen model of length 78 indicated by the vertical line. *Right:* The top plot shows the $[P^{(cs)}_{1-loop}]_{\|0}$ function for two extreme cases of cosmological parameters while the bottom plot displays the resulting 1σ and 2σ emulator % error for all 300 cosmologies. The seemingly large errors for $k < 0.3 h\mathrm{Mpc}^{-1}$ are inconsequential as $[P_{2-\mathrm{loop}}]_{\|0}$ dominates there; see discussion in 3.3.2.

B6 The $[P^{(\mathrm{quad})}_{1-\mathrm{loop}}]_{\|0}$ emulator

For the $[P^{(\mathrm{quad})}_{1-\mathrm{loop}}]_{\|0}$ emulator we chose a model of length 72. We show the Pareto front of RMSE vs model length on the left of Fig.B6. The resulting function is

$$
\frac{[P^{(\mathrm{quad})}_{1-\mathrm{loop}}]_{\|0}}{\bar{A}_s^2} = \left[\cos\left(C_{18}\Omega_b - \frac{C_{19}h}{\sqrt{(C_{20}\Omega_b + C_{21}k)^2 + 1}\sqrt{\cos^2\left(\frac{C_{22}\Omega_{cb}}{\sqrt{C_{23}\bar{A}_s^2+1}}\right) + 1}} \right) - \frac{C_{24}\Omega_{cb} + C_{25}k + \cos\left(C_{26}\Omega_{cb} - C_{27}\Omega_b - C_{28}n_s - C_{29}\right)}{\sqrt{(C_{30}\Omega_b + C_{31}k)^2 + 1}} \right]
$$
$$
\times \frac{(C_0 h)^{-C_1\Omega_b - \frac{C_5}{\sqrt{C_6 k^2+1}} + \frac{C_2 h + C_3 n_s}{\sqrt{C_4 h^2+1}}}}{\sqrt{C_{32}k^2 + 1}} (C_7 k)^{\frac{C_9\Omega_{cb}}{\sqrt{(C_{10}\Omega_{cb}+C_{11}k)^2+1}} + \frac{C_{12}\Omega_{cb}}{\sqrt{C_{13}k^2+1}} - C_{14}\Omega_b + C_{15}h + C_{16}n_s + C_{17}k + C_8\Omega_{cb}} - C_{33} \qquad (\text{B11})
$$

where

$C_0 = 1.0114$	$C_1 = 9.199$	$C_2 = 12.811$	$C_3 = 4.371$	$C_4 = 11.248$	
$C_5 = 1.9858$	$C_6 = 29.86$	$C_7 = 12.475$	$C_8 = 1.6152$	$C_9 = 6.5046$	$C_{10} = 3.873$
$C_{11} = 11.89$	$C_{12} = 0.5958$	$C_{13} = 0.0837$	$C_{14} = 5.748$	$C_{15} = 0.4183$	$C_{16} = 1.7877$
$C_{17} = 0.01105$	$C_{18} = 5.0913$	$C_{19} = 3.467$	$C_{20} = 16.01$	$C_{21} = 4.183$	$C_{22} = 6.48$
$C_{23} = 0.05$	$C_{24} = 17.557$	$C_{25} = 1.23$	$C_{26} = 13.345$	$C_{27} = 19.93$	$C_{28} = 0.334$
$C_{29} = 4.051$	$C_{30} = 24.483$	$C_{31} = 1.3545$	$C_{32} = 2.85$	$C_{33} = 8 \times 10^{-4}$	(B12)

This paper has been typeset from a TEX/LATEX file prepared by the author.

Figure B6. *Left:* The Pareto front of RMSE vs model length for the $\frac{[P^{(quad)}_{1loop}]_{\parallel 0}}{\tilde{A}^2_s}$ emulator runs as generated by `Operon`, with blue marking the training and red the validation error, and with the chosen model of length 72 indicated by the vertical line. *Right:* The top plot shows the $[P^{(\text{quad})}_{1-loop}]_{\parallel 0}$ function for two extreme cases of cosmological parameters while the bottom plot displays the resulting 1σ and 2σ emulator % error for all 300 cosmologies. The seemingly large errors for $k < 0.3h\text{Mpc}^{-1}$ are inconsequential as $[P_{2-\text{loop}}]_{\parallel 0}$ dominates there; see discussion in 3.3.2.